arXiv:1612.03818v1 [physics.plasm-ph] 12 Dec 2016

A new hybrid code (CHIEF) implementing the inertial electron fluid equation without approximation

P. A. Muñoz,[1,2,a)] N. Jain,[1,2] P. Kilian,[3] and J. Büchner[1,2]

[1)] *Max-Planck-Institut für Sonnensystemforschung, D-37077 Göttingen, Germany*

[2)] *Max-Planck/Princeton Center for Plasma Physics*

[3)] *Centre for Space Research, North-West University, 2520 Potchefstroom, South Africa*

(Dated: December 13, 2016)

We present a new hybrid code (CHIEF) with kinetic ions modelled using the Particle-in-Cell (PiC) method, and a massive electron fluid adapting the full electron-MHD (EMHD) model. This kind of code is appropriate to model a large variety of quasineutral phenomena where kinetic electron effects can be neglected, but full ion kinetic effects are considered. Different from most other hybrid codes with massless electrons, our model considers properly, without approximations, the full electron inertial effects, relevant in, e.g., scenarios like magnetic reconnection, where it can break the frozen-in condition of ideal MHD. We present here the governing equations of the model, how these are discretized and implemented numerically, as well as six test problems to validate our numerical approach. They are mostly 1D problems where the ion kinetic effects play the essential role. Our chosen test problems are: 1) parallel (to a background magnetic field) propagating electromagnetic waves, 2) perpendicular propagating electrostatic waves (ion Bernstein modes), 3) ion beam right-hand instability (resonant and non-resonant), 4) ion Landau damping, 5) ion firehose instability, and 6) 2D oblique ion firehose instability. Our results reproduce successfully the predictions of linear and non-linear theory for all these problems, validating our code. All properties of this hybrid code make it ideal to study multi scale phenomena between electron and ion scales involving dissipation and turbulence in a more efficient way than traditional, fully kinetic approaches.

[a)] Electronic mail: munozp@mps.mpg.de

I. INTRODUCTION

Fully kinetic simulations, either via Lagrangian Particle-in-Cell (PiC)[1–3] or Eulerian Vlasov[4,5] methods, have become the standard tools to study kinetic plasma phenomena. They are essential to model self-consistently the dissipation at small scales and the multiscale processes in a wide variety of scenarios, often related with turbulence. But these simulations codes tend to be computationally very expensive, which hinders their applicability to many practical problems.

On the other hand, fluid models are used to model phenomena either on large scales and long timescales, like MHD codes, or even on small space and timescales under appropriate conditions, like electron MHD (EMHD) codes[6,7]. Even though they are computationally more convenient than kinetic models, they cannot model self-consistently dissipation, particle acceleration, resonant processes or phenomena related with deviations from the thermal equilibrium or quasineutrality.

Hybrid codes bridge the gap between those different approaches and spatial/time scales. A large number of problems require kinetic effects of ions and fluid descriptions of electrons. This is especially true at frequencies lower than the ion cyclotron Ω_{ci} or spatial scales much larger than the ion skin depth d_i, which are computationally expensive to simulate with fully-kinetic codes. Problems of this class are related to planetary magnetospheres and their associated collisionless shocks, collisionless magnetic reconnection, the acceleration of heavy ions by shocks and reconnection, instabilities driven by ion temperature anisotropy and turbulence in the kinetic dissipation range in the solar wind, among many other ones. In many of these scenarios, the gradient scales of different physical quantities can be very small, which requires the need of considering an electron fluid with finite mass.

In order to study these problems, we present a hybrid code using kinetic ions modeled via PiC methods, and a massive electron fluid using a modified EMHD model. We call it CHIEF: Code Hybrid with Inertial Electron Fluid. By not considering electron kinetic effects and going to the radiation-free limit, we can bypass the stringent stability conditions of a fully kinetic approach, making it computationally cheaper. Our code follows the standard quasineutral approach used in the kinetic hybrid codes, i.e., the electron and ion densities are always equal, eliminating thus the radiation part in the Maxwell's equation associated with the displacement current, light wave propagation (and the corresponding CFL condition

of standard fully-kinetic codes) and other phenomena involving charge separation such as Langmuir waves. On the other hand, and different from other hybrid codes with massless electrons (see, e.g., the review Ref. 8 or the textbook Ref. 9 and references therein), we consider without approximations all the electron inertial terms in the Ohm's law. Note that the inclusion of electron inertia reduces the numerical instability (at short wavelengths) known for hybrid codes with massless electrons. This instability is due to the increase of the phase speed of whistler waves without bound, since $\omega \propto k^2$ in that limit, where ω is the frequency and k the wave number. All these features make our code ideal to deal with fast evolving phenomena at electron scales, which can break the frozen-in condition of ideal MHD allowing processes like magnetic reconnection.

Note that our main approximation is the choice of constant temperature as equation of state for the electrons. Other equations of state such as the polytropic one, where the electron pressure has an explicit dependence on other variables such as the density, can be straightforwardly implemented. On the hand, numerical solutions to equations for the evolution of the electron pressure require additional numerical considerations (like numerical viscosity, see Ref. 10), and in particular if non-gyrotropic contributions are considered, which require a heuristic isotropization term to take into account electron temperature anisotropy driven instabilities (see Ref. 11).

In order to make the advantages of our code clear, let us briefly discuss the different approaches that previous hybrid codes have taken to implement the relevant electron fluid equations and their coupling with Maxwell's equations. Even since the early days of the development of (PiC-)hybrid codes, electron inertia has been considered to deal with fast phenomena close to the electron cyclotron frequency, as demonstrated by an early 1D electrostatic code.[12] A 2.5D electromagnetic hybrid code was developed by Ref. 13, allowing some electron mass effects. Those codes[12,13] implemented the quasineutral approximation by using the radiation-free (Darwin) limit of the Maxwell's equations. Correspondingly, they used a Helmholtz decomposition by solving separately the longitudinal and transverse parts of the electromagnetic potentials and current density. Longitudinal/transverse refers to the curl-free/divergence-free part of the corresponding fields, and not to physical directions in space. The electron inertia was considered in the equation for the transverse electron current density. An evolution equation for the electron temperature including terms up to the heat flux was considered. This method involved solving several elliptic equations for the

fields (with the form of generalized Poisson's equations). Hybrid codes based on potentials, however, have been rarely used since then, excepting 1D cases which use the electrostatic potential. One example is the 1D code developed in Ref. 14, which modelled a highly collisional plasma typical of pressure discharges with a complex chemistry. It consists of fully-kinetic electrons (using Monte-Carlo methods take into account collisions) and several species of heavy ions modelled with a fluid approach.

Much later, Ref. 15 proposed a (2.5D) hybrid code algorithm to simulate the entire Earth's magnetosphere. To do so, it included a cold ion fluid component to take into account the ionospheric plasma, as well as curvilinear coordinates. In this approach, the electric field is determined from the electron momentum equation with electron inertia, while the electron velocity from the Ampère's law and the magnetic field from the Faraday's law. No electron pressure term was considered in the electron momentum equation. The electron inertia term was only considered as a correction in the form of an electron polarization drift in the (implicit) equation for the magnetic field, while neglected in all the other equations. This has the advantage, however, of making the entire code explicit. This code was applied to the substorm onset and other magnetospheric scenarios in Ref. 16.

After that, the standard approach in inertial hybrid codes has been to solve equations for generalized electromagnetic fields (Sec. 5.7 in Ref. 9, Refs. 10 and 17). In this approach, the electromagnetic fields are obtained from a generalized magnetic $\hat{\vec{B}}$ and electric $\hat{\vec{E}}$ fields which satisfy a Faraday's-like equation. Those 2.5D hybrid codes have been used to study collisionless magnetic reconnection[18–20]. The equations for the generalized fields $\hat{\vec{B}}$ and $\hat{\vec{E}}$ were solved by using a predictor-correct scheme (which requires a staggered grid) or a trapezoidal leapfrog algorithm. As discussed in detail later, the electromagnetic fields are obtained from the generalized fields under varying approximations. Spatio-temporal density variations on electron scales and time derivative of the ion current were neglected in the expression for $\hat{\vec{B}}$ and $\hat{\vec{E}}$, respectively[17]. Although the contribution of electron inertia via the convective electron acceleration term was considered in calculating the electric field $\hat{\vec{E}}$, non-stationary electron inertia was neglected[17]. Some authors neglected even the convective electron acceleration term[10]. On the other hand, Ref. 10, used an evolution equation for an scalar electron pressure, while Ref. 17 included the full electron pressure tensor to take into account the non-gyrotropic effects that were shown to have an important role in balancing the reconnection electric field under some conditions. None of the effects related with an

equation for the evolution of the electron pressure is considered in our code, yet.

A slightly different method to obtain the electric field from $\hat{\vec{E}}$ consists in writing implicitly the equation for the generalized electric field (instead of the magnetic field), combining the Ohm's law with the other Maxwell's equation was also considered, resulting in an elliptic equation for $\vec{E}$ (see Sec. 5.2.4 in Ref. 9). They pointed out that one of the main advantages of this approach is the possibility to simulate regions with large variations in density, something that the previous methods cannot handle easily due to the division by this quantity in several of the Ohm's law terms. The main application of this kind of hybrid codes was to simulate collisionless shocks.

In hybrid codes, the modelling of ions not only can be done via PiC methods, but also via Eulerian Vlasov methods. In this sense, the only example (as far as we are aware) of a (2.5D) hybrid Vlasov code incorporating electron inertia was developed by Ref. 21. This code couples the ion equation of motions, solved by standard splitting methods for the Vlasov equation, with the electromagnetic fields equations calculated via the current advance method (CAM),[22] implying the use of the first ion momenta equation, including a tensor pressure, to advance the ion current and thus to calculate the electric field. The corresponding generalized Ohm's law is a Helmholtz equation for the generalized electric field written in terms of the ion fluid velocity and the ion tensor pressure. It does not involves time derivatives, because of the quasineutral approximation and Faraday's law. The solution of this equation is simplified by assuming small negligible density perturbations in the expression for the electric field. The equation of state for the electrons is assumed to be isothermal. This code by Ref. 21 has been applied to a several problems related to solar wind turbulence (see, e.g., Refs. 23–25).

More recently, Ref. 26 developed a (3D) hybrid code with electron inertia and kinetic ions modelled via the δf method, via a second-order accurate semi-implicit algorithm using a current closure scheme. The δf method consists in evolving only the variations of the ion distribution function, which are assumed to be weak with respect to a given background, and thus to reduce the numerical noise predominant in conventional full-f methods. The electron inertial effects are included in the generalized Ohm's law for the electric field, and are calculated from the Ampère's law and the ion momentum equation. This approach was proposed first on Ref. 27 for the 1D gyrofluid electron equations, which was later applied for investigations on propagation of dispersive Alfvén waves in the Earth's magnetosphere-

ionosphere region and the mechanisms of electron acceleration[28,29], and the Alfvén dynamics in an Io-Jupiter flux tube[30]. The electric field is advanced first by decomposing the Ohm's law into a perturbed and an equilibrium part. The fields are solved in real space for the inhomogeneous direction and in Fourier space for the homogeneous direction. The equilibrium part of the Ohm's law is cast in the form of a linear equation and solved by matrix inversion methods, while the perturbed part is solved iteratively. After that, the magnetic field is obtained explicitly from Faraday's law and finally, the electromagnetic fields can be used to advance the (perturbed) particle distribution. The closure for the electron pressure was chosen via an isothermal equation of state. This code was benchmarked against the (2D) resistive tearing instability, among other (1D) problems.

Finally, the latest hybrid code with electron inertia was published in Ref. 31 (as far as we are aware of). The special feature of this 1D code is that can handle low density and vacuum regions without becoming unstable. In order to do that, a correction term is introduced to the electric instead of the magnetic field, in addition to a variable (ion-to-electron) mass ratio which reduces the phase speed of whistler waves to satisfy the stability conditions everywhere. This is done not only because of the divisions by density in the equation for the electric field, but also because the Alfvén speed is inversely proportional to (the square root of) the density, implying a more stringent condition in the choice of the time step and the relevant CFL condition (related to the electron Alfvén speed). The approach by Ref. 31 consisted in not using the generalized electromagnetic fields as in Refs. 9, 10, and 17, but instead solving a modified form of the Ohm's law for the electric field (without divisions by density) and then obtaining the magnetic field through the Faraday's law. The first equation is solved by matrix methods while the second one by a direct iterative algorithm. The electron inertia effects are considered in both equations with some approximations, however. In the vacuum limit, and following the idea of a previous inertia-less hybrid code[32], the equation for the electric field becomes the Laplace's equation, being easily solvable without numerical singularities as in other approaches due to the division by density. The electron pressure is considered to follow an adiabatic equation of state, with a corresponding evolution equation in case of a finite resistivity (constant otherwise). Finally, the variable mass ratio procedure is done in practice by varying locally and temporally the electron mass, adjusting it to always satisfy the CFL condition based on the electron Alfvén speed for given timestep and grid cell sizes. This works well as long as the scales of interest are not too

close to the electron inertial scales.

This rest of this paper is organized as follows. In Sec. II we present a detailed description of the simulation model used by our code. In Sec III we describe the numerical implementation of our equations. In Sec. IV we show a detailed comparison of simulations results of six test problems with the predictions of linear (and non-linear) theory: 1) parallel (to a background magnetic field) propagating electromagnetic waves, 2) perpendicular propagating electrostatic waves (ion Bernstein modes), 3) ion beam right-hand instability (resonant and non-resonant), 4) ion Landau damping, 5) ion firehose instability and 6) 2D oblique ion firehose instability. These test problems cover different aspects of ion kinetic effects, essential to understand phenomena in a wide variety of laboratory, space and astrophysical plasmas. All the results match within the expected error range. We summarize our results in Sec. V.

II. SIMULATION MODEL

We treat ions as Lagrangian macro-particles modeled via the PiC method and electrons as a (Eulerian) fluid with finite mass and temperature. Each ion macro-particle (index "p") represents a (large) number N_i of physical ions (index "i") according to $f_i^p(\vec{x}_i^{\,p}, \vec{v}_i^{\,p}, t) = N_i^p\, S(\vec{x}_i - \vec{x}_i^{\,p}(t))\delta(\vec{v}_i - \vec{v}_i^{\,p}(t))$, where $\vec{x}_i^{\,p}$, $\vec{v}_i^{\,p}$ are the macro-ions' position, velocity and $S(\vec{x}_i - \vec{x}_i^{\,p}(t))$ is called the shape function (see details in Sec. III). The (physical) ion distribution function is obtained as the summation over all ion-macroparticles $f_i(\vec{x}_i, \vec{v}_i, t) = \sum_p N_i^p\, S(\vec{x}_i - \vec{x}_i^{\,p}(t))\delta(\vec{v}_i - \vec{v}_i^{\,p}(t))$. In the collisionless plasmas to be considered, this macro-ion distribution function f_i^p evolves according to a similar Vlasov equation governing the full ion distribution function f_i (see, e.g., Ref. 33):

$$\frac{\partial f_i^p}{\partial t} + \vec{v}_i \cdot \frac{f_i^p}{\partial \vec{x}_i} + \frac{Ze}{m_i}\left(\vec{E} + \vec{v}_i \times \vec{B}\right) \cdot \frac{\partial f_i^p}{\partial \vec{v}_i} = 0. \tag{1}$$

Here, Ze and m_i are the charge (with e the fundamental charge) and mass of a physical ion, respectively. By taking the first order momenta in $\vec{x}_i$ and $\vec{v}_i$ of Eq. (1) (i.e., multiplying and integrating Vlasov equation by $\iint \vec{x}_i\,(\text{Eq. (1)})\, d\vec{x}_i\, d\vec{v}_i$ and $\iint \vec{v}_i(\text{Eq. (1)})\, d\vec{x}_i\, d\vec{v}_i$, respectively. See details in, e.g., Ref. 33), one obtains the equations of motion of the macro-ions (setting

$Z = 1$, i.e., singly charged ions, for simplicity):

$$\frac{d\vec{x}_i^{\,p}}{dt} = \vec{v}_i^{\,p}, \tag{2}$$

$$m_i \frac{d\vec{v}_i^{\,p}}{dt} = e(\vec{E}_i^{\,p} + \vec{v}_i^{\,p} \times \vec{B}_i^{\,p}). \tag{3}$$

where $\vec{x}_i^{\,p}$ and $\vec{v}_i^{\,p}$ are the first momenta in $\vec{x}_i$ and $\vec{v}_i$ of f_i^p, respectively. These equations resemble Newton's equation of motion for the macroparticles, with the difference that $\vec{E}_i^{\,p}$ and $\vec{B}_i^{\,p}$ are calculated integrating the full electromagnetic fields over the shape function $S(\vec{x} - \vec{x}_i^{\,p}(t))$ (see Eqs. (11)-(12)). The code actually solves the relativistic version of these equations, obtained by replacing $\vec{v}_i$ by $\vec{u} = \gamma\vec{v}_i$, with $\gamma = (1 - v_i^2/c^2)^{-1/2}$ the relativistic gamma factor. But relativistic effects can be safely neglected for the regime appropriate for a quasineutral hybrid code ($v_i \ll c$, with c the speed of light). The ion density n_i, ion bulk velocity $\vec{u}_i$ and the ion current density $\vec{j}_i$ are obtained as the two first order velocity momenta of the ion distribution function $f_i(\vec{x}_i, \vec{v}_i)$, i.e., $n_i = \int f_i \, d^3\vec{v}$ and $\vec{j}_i = e \int \vec{v}_i \, f_i \, d^3\vec{v} = e n_i \vec{u}_i$ (see details on the implementation in Sec. III). With a similar procedure it is possible to obtain higher order momenta such as the ion pressure tensor (associated with the ion temperature).

For fluid electrons, we consider the electron momentum equation with finite electron inertia and resistive effects, that is a generalized Ohm's law for the electric field:

$$\vec{E} = -\vec{u}_e \times \vec{B} - \frac{1}{e n_e} \frac{\partial P_{e,jk}}{\partial x_k} - \frac{m_e}{e} \left(\frac{\partial \vec{u}_e}{\partial t} + (\vec{u}_e \cdot \vec{\nabla}) \vec{u}_e \right) + \eta \vec{j}. \tag{4}$$

Here, $\eta = m_e \nu / (e^2 n_e)$ is the the collisional resistivity with ν the collision frequency (between electrons and ions), $\vec{j} = e(n_i \vec{u}_i - n_e \vec{u}_e)$ is the total density current, $\vec{u}_e$ is the electron fluid velocity and $P_{e,jk}$ is the jk component of the electron pressure tensor. Note that k is a summation index, in such a way that $\partial P_{e,jk}/\partial x_k$ represents the $j = x, y, z$ component.

The electric and magnetic fields are related to the plasma current via the Faraday's law and Ampère's law without displacement current:

$$\vec{\nabla} \times \vec{E} = -\frac{\partial \vec{B}}{\partial t}, \tag{5}$$

$$\vec{\nabla} \times \vec{B} = \mu_0 \, n \, e(\vec{u}_i - \vec{u}_e). \tag{6}$$

Note that neglecting the displacement current in Eq. (6) is equivalent to set the dielectric constant $\epsilon_0 \to 0$, preventing light (and Langmuir) wave propagation and assuming quasi-neutrality $n_e = n_i = n$ for this parameter regime, with $n_{(e/i)}$ the electron/ion density,

respectively. This condition implies the restriction to frequencies much smaller than the electron plasma frequency $\omega \ll \omega_{pe}$ and length-scales much larger than the Debye length $\lambda \gg \lambda_{De}$. The Poisson's equation $\vec{\nabla} \cdot \vec{E} = e(n_i - n_e)/\epsilon_0$ is automatically satisfied because of the quasi-neutral approximation and boundary conditions, while $\vec{\nabla} \cdot \vec{B} = 0$ is also fulfilled if the initial conditions satisfies it.[8]

Combining the electron momentum Eq. (4) and Faraday's law Eq. (5), we can eliminate the electric field and obtain an evolution equation for the magnetic field, which has the form of a generalized continuity equation,

$$\frac{\partial \overrightarrow{W}}{\partial t} = \vec{\nabla} \times \left[\vec{u}_e \times \overrightarrow{W} \right] - \vec{\nabla} \times \left(\frac{\vec{\nabla} p_e}{m_e n_e} \right) - \vec{\nabla} \times \left(\frac{\nu}{e n_e} \vec{j} \right), \tag{7}$$

where

$$\overrightarrow{W} = \vec{\nabla} \times \vec{u}_e - e\vec{B}/m_e, \tag{8}$$

is the generalized vorticity. For simplicity, we have assumed a scalar electron pressure p_e given by the isothermal equation of state,

$$p_e = \frac{1}{3} P_{e,kk} = n_e k_B T_e, \tag{9}$$

with k_B is the Boltzmann constant and T_e is the electron temperature, constant in time. Note that if the temperature T_e and density n_e are spatially uniform, the second term in Eq. (7) vanishes.

In conventional hybrid codes with electron inertia[9,10,17], the electric field is obtained from Eq. (4) while the magnetic field is obtained from Eqs. (7) and (8). This is done, however, by neglecting some terms. Substituting for $\vec{u}_e$ from Eq. (6) and neglecting terms proportional to $\partial \vec{u}_i/\partial t$ and $\partial n_e/\partial t$ and electron-scale spatial variations of the density, the l.h.s. (left hand side) of Eq. (7) can be written entirely in terms of the time derivative of the magnetic field, i.e., as $\partial/\partial t[e(\vec{B} - d_e^2 \vec{\nabla}^2 \vec{B})/m_e]$, where $d_e = c/\omega_{pe}$ is the electron inertial length. The magnetic field is then obtained by solving an elliptic equation for $\vec{B}$. Neglecting $\partial \vec{u}_i/\partial t$ and $\partial n_e/\partial t$ in Eq. (7) is justified for a large mass ratio m_i/m_e. However, these approximations are not necessarily valid in all the situations of interest and need to be checked for each case, especially for simulations using an artificially low mass ratio m_i/m_e. The electric field is calculated directly from the electron momentum Eq. (4) by neglecting $\partial \vec{u}_e/\partial t$, which is clearly inconsistent with keeping this term in Eq. (7).

In our hybrid simulation model, we solve Eqs. (2)-(9) without making any of these approximations. Eq. (7) is solved for the generalized vorticity $\overrightarrow{W}$ and then, the magnetic field is calculated from an elliptic equation obtained by combining Eq. (8) with Ampère's law Eq. (6),

$$\frac{1}{\mu_0 e}\vec{\nabla}\times\left(\frac{\vec{\nabla}\times\vec{B}}{n_e}\right)+\frac{e\vec{B}}{m_e}=\vec{\nabla}\times\vec{u}_i-\overrightarrow{W}. \tag{10}$$

Note that in Eq. (10) we do not neglect the density variations at electron scales, and explicitly calculate the curl of the ion bulk velocity. Next, the electric field is calculated from the electron momentum Eq. (4) (in the form of a generalized Ohm's law) by explicitly evaluating the time derivative term $\partial\vec{u}_e/\partial t$. For this purpose, we assume that ions quantities do not change much in a single time step, which is a small fraction of the electron gyroperiod. Thus, for a single time step (Δt) of the simulation, $\vec{u}_e$ is obtained at $t_1 = t_0 + \Delta t$ and $t_2 = t_0 + 2\,\Delta t$ by advancing Eq. (7) in two steps of length Δt from t_0 to t_2. This allows the calculation of $\partial\vec{u}_e/\partial t$ at t_1 by a central finite difference scheme. In the second of the two time steps, the code reuses the same ions quantities n_i and $\vec{j}_i$ used in the first time step (with index t_1).

III. NUMERICAL IMPLEMENTATION

The simulation model discussed in Sec. II is numerically implemented by combining a particle-in-cell (PiC) code, ACRONYM[34], with an electron-magnetohydrodynamics (EMHD) code[7,35]. Both codes have been tested independently and used in the past for simulations of magnetic reconnection[36,37], instabilities[38,39], particle acceleration via instabilities[40], CME-driven shocks[41], wave coupling[42], resonant wave-particle interaction[43], etc. Fig. 1 shows a scheme of the numerical implementation and coupling of the two codes.

On the PiC side of the code, the electromagnetic fields are assumed to be known at the staggered grid called the Yee lattice.[44] They are, however, provided by the EMHD side of the code on a grid where all quantities are defined at cell centers except the magnetic field which is defined at the edges of each cell. Therefore, we employ an interpolation procedure between the two grids schematized in Fig. 2, in order to align correctly those quantities in the Yee lattice. Once the electromagnetic fields are interpolated from the EMHD to the PiC cell, the following steps (shown in Fig. 1) are taken to move the particles:

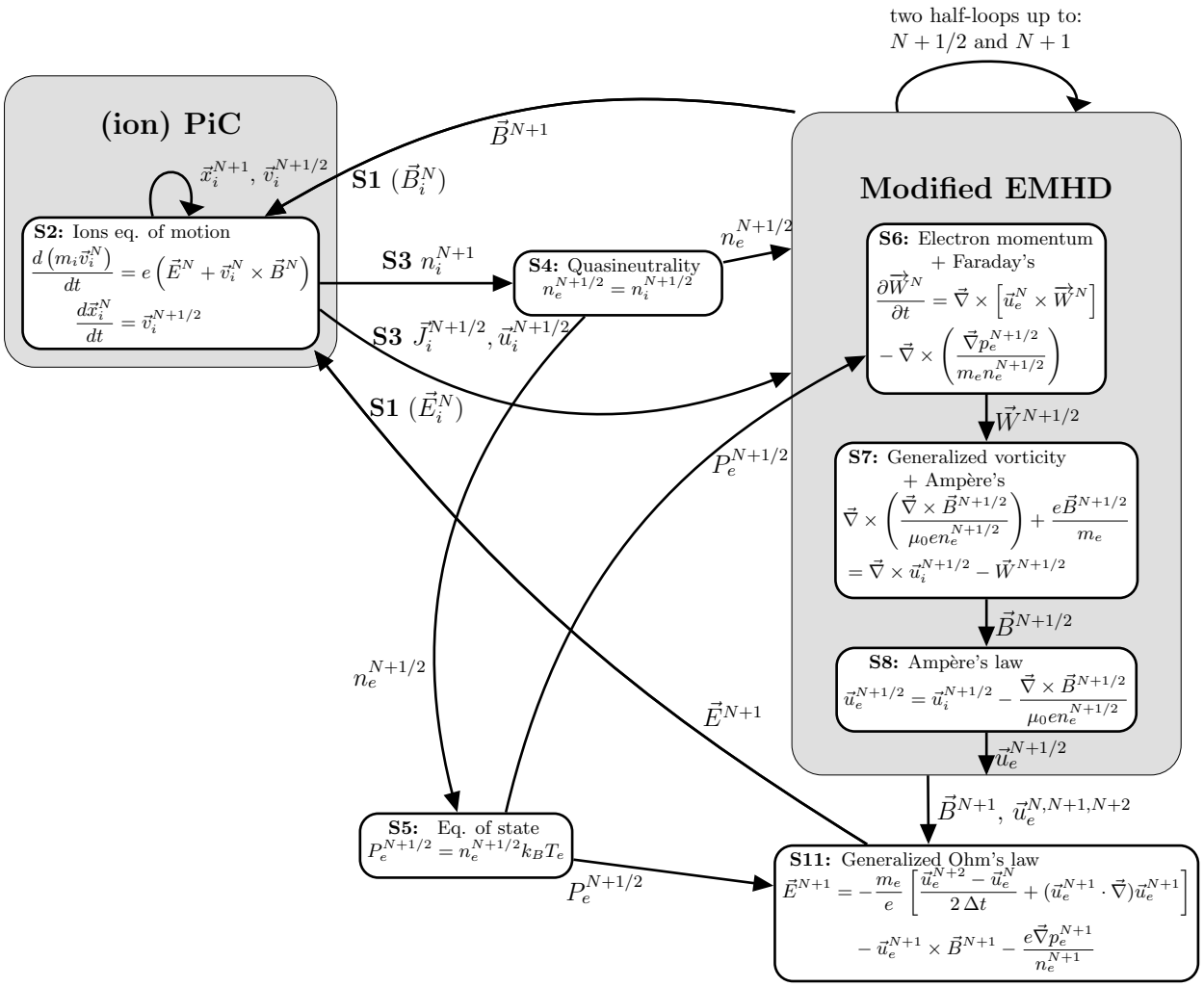
two half-loops up to:
$N+1/2$ and $N+1$
(ion) PiC
$\vec{x}_i^{N+1}$, $\vec{v}_i^{N+1/2}$
$\vec{B}^{N+1}$
S1 $(\vec{B}_i^N)$
S2: Ions eq. of motion
$\frac{d\left(m_i\vec{v}_i^N\right)}{dt} = e\left(\vec{E}^N + \vec{v}_i^N \times \vec{B}^N\right)$
$\frac{d\vec{x}_i^N}{dt} = \vec{v}_i^{N+1/2}$
S3 n_i^{N+1}
S4: Quasineutrality
$n_e^{N+1/2} = n_i^{N+1/2}$
$n_e^{N+1/2}$
S3 $\vec{J}_i^{N+1/2}$, $\vec{u}_i^{N+1/2}$
S1 $(\vec{E}_i^N)$
Modified EMHD
S6: Electron momentum + Faraday's
$\frac{\partial \vec{W}^N}{\partial t} = \vec{\nabla} \times \left[\vec{u}_e^N \times \vec{W}^N\right] - \vec{\nabla} \times \left(\frac{\vec{\nabla} p_e^{N+1/2}}{m_e n_e^{N+1/2}}\right)$
$\vec{W}^{N+1/2}$
S7: Generalized vorticity + Ampère's
$\vec{\nabla} \times \left(\frac{\vec{\nabla} \times \vec{B}^{N+1/2}}{\mu_0 e n_e^{N+1/2}}\right) + \frac{e\vec{B}^{N+1/2}}{m_e} = \vec{\nabla} \times \vec{u}_i^{N+1/2} - \vec{W}^{N+1/2}$
$\vec{B}^{N+1/2}$
S8: Ampère's law
$\vec{u}_e^{N+1/2} = \vec{u}_i^{N+1/2} - \frac{\vec{\nabla} \times \vec{B}^{N+1/2}}{\mu_0 e n_e^{N+1/2}}$
$\vec{u}_e^{N+1/2}$
$P_e^{N+1/2}$
$n_e^{N+1/2}$
$\vec{E}^{N+1}$
$\vec{B}^{N+1}$, $\vec{u}_e^{N,N+1,N+2}$
S5: Eq. of state
$P_e^{N+1/2} = n_e^{N+1/2} k_B T_e$
$P_e^{N+1/2}$
S11: Generalized Ohm's law
$\vec{E}^{N+1} = -\frac{m_e}{e}\left[\frac{\vec{u}_e^{N+2} - \vec{u}_e^N}{2\,\Delta t} + (\vec{u}_e^{N+1} \cdot \vec{\nabla})\vec{u}_e^{N+1}\right] - \vec{u}_e^{N+1} \times \vec{B}^{N+1} - \frac{e\vec{\nabla} p_e^{N+1}}{n_e^{N+1}}$

Figure 1. Scheme of the equations of our hybrid simulation code developed by coupling a PiC and an EMHD code. "Sx" stands for step number x (explained in the text).

A. Particle mover (PiC part)

The PiC side of the hybrid code, as done in all fully-kinetic PiC codes, including ACRONYM, updates ion velocities and positions in the given electric and magnetic fields $\vec{E}_i^N$ and $\vec{B}_i^N$ known at the time index N.

- **Step 1:** The electromagnetic fields are interpolated from the grid to the the macro-

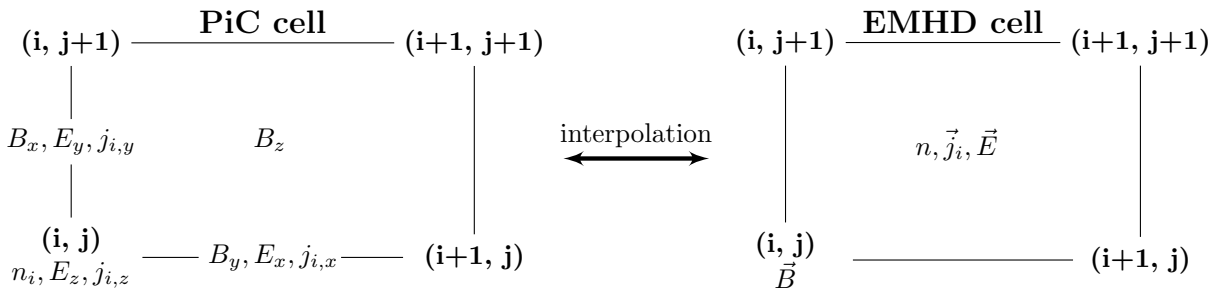

Figure 2. Scheme of the allocations of different physical quantities in the grids associated to the PIC (Yee lattice) and EMHD parts of the hybrid code. For simplicity, only the 2D case is shown. The indices of the grid points are indicated in the vertices of the cell (i for the x direction and j for the y direction).

particle positions with a weighting given by the shape function $S(\vec{x}_i - \vec{x}_i^{\,p})$:

$$\vec{E}_i^{\,p} = \vec{E}(\vec{x}_i^{\,p}) = \int \vec{E}(\vec{x}_i)\, S(\vec{x}_i - \vec{x}_i^{\,p})\, d\vec{x}_i, \tag{11}$$

$$\vec{B}_i^{\,p} = \vec{E}(\vec{x}_i^{\,p}) = \int \vec{B}(\vec{x}_i)\, S(\vec{x}_i - \vec{x}_i^{\,p})\, d\vec{x}_i, \tag{12}$$

where the subscript p indicates the location of each (macro-)particle. In the code, the interpolations between the EMHD and PiC grid and from the PiC grid to macro-particle's position are combined in a single operation.

- **Step 2:** Then, the ions can be moved via the second-order accurate leap-frog algorithm, which means that at each timestep N, the ion velocities are advanced from the half-timestep $N - 1/2$ to the half-timestep $N + 1/2$ and the ion positions from the timestep N to the timestep $N + 1$ by using the discretized version of Eqs. (2) and (3) (see, e.g., Ref. 1):

$$\vec{x}_i^{\,p,N+1} = \vec{x}_i^{\,p,N} + \vec{v}_i^{\,p,N+1/2} \Delta t, \tag{13}$$

$$\vec{v}_i^{\,p,N+1/2} = \vec{v}_i^{\,p,N-1/2} + \frac{e}{m_i} \left(\vec{E}_i^{\,p,N} + \frac{\vec{v}_i^{\,p,N+1/2} + \vec{v}_i^{\,p,N-1/2}}{2} \times \vec{B}_i^{\,p,N} \right) \Delta t. \tag{14}$$

Note that the first equation is explicit while the second implicit. We advance the ion velocity via the Boris method[45], which involves a rotation of $\vec{v}_i^{\,N+1/2}$ making Eq. (14) also explicit.

- **Step 3:** Because of the staggering of the position and velocity updates, the sources of the electromagnetic field, the ion number density n_i and current density $\vec{j}_i$, are

computed at the time index $N+1$ and $N+1/2$, respectively. This deposition is done via an interpolation scheme using the same shape function as for the electromagnetic field interpolation from the grid to macro-particle's position (Eqs. (11)-(12)):

$$n_i^{N+1}(\vec{x}_i) = \sum_p N_p \, S(\vec{x}_i - \vec{x}_i^{\,p,N+1}), \tag{15}$$

$$\vec{j}_i^{\,N+1/2}(\vec{x}_i) = \sum_p N_p \, \vec{v}_i^{\,p,N+1/2} S(\vec{x}_i - \vec{x}_i^{\,p,N+1}). \tag{16}$$

The code has available, at compilation time, an option to smooth both quantities by performing a binomial filter and, if required, a compensation pass[46]. Note that, different from ACRONYM and other state-of-the-art fully-kinetic PiC codes, we do not need to use the charge-preserving Esirkepov scheme[47] to deposit the current $\vec{j}_i$ onto the grid, due to the quasineutrality condition of the hybrid approach[48]. On the other hand, the reason to use the same shape function in Eqs. (15) and (11) is to avoid self-forces and preserve the global momentum.[49] Our hybrid code has, as inherited from ACRONYM, the following shape functions available: NGP (Nearest Grid Point), CIC (Cloud in Cell), TSC (Triangular Shaped Cloud), PQS (Piecewise Quadratic Spline) and other ones, useful under some specific conditions. By default, we use the second order shape function TSC to reduce the intrinsic PiC shot noise without affecting the computational performance too much.

Once the sources of the electromagnetic fields in Eq. (15)-(16) are known at the Yee lattice, they are passed and interpolated to the EMHD grid following the inverse procedure as in Fig. 2 (similarly as before, it is actually combined with the deposition in Eq. (15)). Then, the EMHD part of the code updates the electromagnetic fields by using the electron fluid and Maxwell's equations described later. The updated electric and magnetic fields are then passed back to the PiC side and the cycle continues.

B. Field updater (EMHD part)

After step 3 in Fig. 1, just before entering into the EMHD part of the code, the input quantities are known at the following time indices: $\vec{E}^N$, $\vec{B}^N$, $\vec{j}^{N+1/2}$ and n_i^{N+1}. The ion density is also calculated at the same index $N+1/2$, $n_i^{N+1/2}$, by taking the average values of n_i^N and n_i^{N+1}.

- **Step 4:** The quasineutrality condition is applied to get $n_e^{N+1/2}$.

- **Step 5:** With $n_e^{N+1/2}$ and a specified value of the electron temperature T_e (which is constant and does not evolve in time), the code computes the electron pressure $p_e^{N+1/2} = n_e^{N+1/2} k_B T_e$ via the equation of state, Eq. (9).

- **Step 6 (first half-loop):** In order to update the electric and magnetic fields, the generalized vorticity $\overrightarrow{W}$ Eq. (7) is advanced from timestep N to $N+1$ by using a flux-corrected transport algorithm[50] of the LCPFCT package[51]. The full update to the next timestep ($\overrightarrow{W}^{N+1}$) requires $\overrightarrow{W}^{N+1/2}$ and $\vec{u}_e^{N+1/2}$ which are not known yet. Because of this, the field solver first advances the generalized vorticity $\vec{W}^N$ by half a timestep (with the input quantities $n_e^{N+1/2}$, $p_e^{N+1/2}$, $\vec{u}_e^N$, $\vec{W}^N$, $\vec{B}^N$) to estimate $\vec{u}_e^{N+1/2}$, $\vec{W}^{N+1/2}$, and $\vec{B}^{N+1/2}$, by solving the discretized version of Eq. (7):

$$\left.\frac{\partial \overrightarrow{W}}{\partial t}\right|_{N\to N+1/2} = \vec{\nabla} \times \left[\vec{u}_e^N \times \overrightarrow{W}^N\right] - \vec{\nabla} \times \left(\frac{\vec{\nabla} p_e^{N+1/2}}{m_e n_e^{N+1/2}}\right). \tag{17}$$

  A multi-dimensional time operator splitting is used to solve this equation by decomposing it in three one-dimensional sub-equations, one for each component (see, e.g., Sec. 5.3.1 of Ref. 9). The sub-equation for a given direction of integration is obtained by keeping the derivatives only in that direction. Then, step 6 to step 8 are performed for each direction of integration.

- **Step 7 (first half-loop):** Next, the solution for $\vec{B}^{N+1/2}$ of the discretized version of the elliptic Eq. (10) is obtained,

$$\vec{\nabla} \times \left(\frac{\vec{\nabla} \times \vec{B}^{N+1/2}}{\mu_0 e n^{N+1/2}}\right) + \frac{e\vec{B}^{N+1/2}}{m_e} = \vec{\nabla} \times \vec{u}_i^{N+1/2} - \vec{W}^{N+1/2}. \tag{18}$$

  Its solution allows to obtain $\vec{B}^{N+1/2}$ from $\vec{W}^{N+1/2}$. This elliptic partial differential equation (PDE) is solved by the subroutines provided by the MUDPACK 5.0 libraries[52], which use multigrid iteration[53,54]. In particular, the form of the equation is appropriate to be solved via the "mud2/3" subroutine, which is a second-order difference approximation for non-separable PDEs on a rectangular/cubic domain (for 2D/3D cases, respectively).

- **Step 8 (first half-loop):** The next step consists in obtaining the components of $\vec{u}_e^{N+1/2}$ (actually, the components y and z) from the discretized form of Ampere's law

Eq. (6):

$$\vec{u}_e^{N+1/2} = \vec{u}_i^{N+1/2} - \frac{\vec{\nabla} \times \vec{B}^{N+1/2}}{\mu_0 e n_e^{N+1/2}}. \tag{19}$$

- **Step 9: Steps 6-8, second half-loop:** At this point of time, the code knows all relevant quantities at the time index $N+1/2$, i.e., $\vec{u}_e^{N+1/2}$, $\vec{B}^{N+1/2}$ and $\vec{W}^{N+1/2}$. Then, all these quantities are advanced to the time index $N+1$, by repeating the steps 6 to 8 in Fig. 1. Explicitly, the equations to be solved in this second half-loop are obtained from:

$$\left.\frac{\partial \vec{W}}{\partial t}\right|_{N+1/2 \to N+1} = \vec{\nabla} \times \left[\vec{u}_e^{N+1/2} \times \vec{W}^{N+1/2}\right] - \vec{\nabla} \times \left(\frac{\vec{\nabla} p_e^{N+1/2}}{m_e n_e^{N+1/2}}\right), \tag{20}$$

$$\vec{\nabla} \times \left(\frac{\vec{\nabla} \times \vec{B}^{N+1}}{\mu_0 e n_e^{N+1/2}}\right) + \frac{e\vec{B}^{N+1}}{m_e} = \vec{\nabla} \times \vec{u}_i^{N+1/2} - \vec{W}^{N+1}, \tag{21}$$

$$\vec{u}_e^{N+1} = \vec{u}_i^{N+1/2} - \frac{\vec{\nabla} \times \vec{B}^{N+1}}{\mu_0 e n_e^{N+1/2}}. \tag{22}$$

With this, we have the quantities $\vec{u}_e^{N+1}$, $\vec{B}^{N+1}$ and $\vec{W}^{N+1}$. Note that we have used the ion quantities ($\vec{u}_i$ and n_i) at the time index $(N+1/2)$, same as the for the first half-loop. This is justified by the heavy mass of the ions compared to the electrons.

The two half-loops described before (twice the steps 6 to 8) are repeated for the integration in each one of the spatial directions x, y and z (in case of a 3D configuration), obtaining thus the time evolution of the relevant quantities due to the spatial derivatives in each direction.

- **Steps 10: Steps 6-9, full-loop, second time:** Before calculating the electric field, we repeat the above procedure (Steps 6-9) by advancing the equations from time step $N+1$ to $N+2$ but also using the ion quantities at the time index $N+1/2$ (i.e., assuming that they are temporally fixed). This gives us $\vec{B}^{N+2}$, $\vec{W}^{N+2}$ and $\vec{u}_e^{N+2}$.

- **Step 11:** Now, the electric field at the time step $N+1$ is calculated from the discretized form of the Ohm's law Eq. (4):

$$\vec{E}^{N+1} = -\frac{m_e}{e}\left[\frac{\vec{u}_e^{N+2} - \vec{u}_e^{N}}{2\,\Delta t} + (\vec{u}_e^{N+1} \cdot \vec{\nabla})\vec{u}_e^{N+1}\right] - \vec{u}_e^{N+1} \times \vec{B}^{N+1} - \frac{\vec{\nabla} p_e^{N+1}}{e n_e^{N+1}}. \tag{23}$$

We use the value of $p_e^{N+1} = n_e^{N+1} k_B T_e$ provided by the equation of state Eq. (9) in the same way as before (steps 4 and 5 in Fig. 1). Note that we have assumed $p_e^{N+1} = p_e^{N+1/2}$ and $n_e^{N+1} = n_e^{N+1/2}$.

Finally, the values of $\vec{E}^{N+1}$ and $\vec{B}^{N+1}$ are passed to the PiC side of the hybrid code, which now provides $\vec{j}_i^{N+3/2}$ and n_i^{N+2}. This ends a timestep and the cycle is repeated for the following one.

IV. TEST PROBLEMS

In the following we describe the six test problems used to validate our numerical method.

Test problem	m_i/m_e	V_A/c	β_i	T_i/T_e
Parallel EM modes	100	10^{-4}	$\{0.01, 0.1\}$	1
Ion Bernstein	400	10^{-3}	0.1	1
Ion beam R instability	100	10^{-4}	β_e=0.1	10
Ion Landau damping	100	10^{-3}	2.0	[0.1-0.66]
Ion firehose instability	100	10^{-2}	$300/\pi = 95.5$	1
2D oblique ion firehose instability	100	10^{-3}	2.8	1

Table I. Main physical parameters for the the tests problems. The ion Landau problem is unmagnetized, but we still use a reference magnetic field for calculating β_i and all the normalizations depending on it. We use two values for β_i in the parallel EM modes, and a range of values for T_i/T_e for the ion Landau damping test problem. Since there different β_i for the different components of the ion beam instability, here we give instead β_e.

A. Parallel electromagnetic modes

In the framework of the cold two-fluid plasma model, two basic parallel (to a background magnetic field) propagating electromagnetic waves are the L and R modes. Their name stand for their polarization: L/R for left/right-handed circularly polarized waves, sometimes called ion-cyclotron Alfvén and whistler waves, respectively. These waves have electric and

Test problem	N_x	L_x/d_i	$\Delta x/d_i$	$\Delta t\,\Omega_{ci}$	$T\Omega_{ci}^{-1}$	ppc
Parallel EM modes	1024	102.4	0.1	$5\cdot10^{-3}$	600	512
Ion Bernstein	1920	63.6	0.033	$4\cdot10^{-3}$	600	64
Ion beam R instability	1024	256	0.25	$1\cdot10^{-2}$	120	1024
Ion Landau damping	256	42.24	0.165	$1\cdot10^{-3}$	60	4096
Ion firehose instability	480	300	0.625	$1\cdot10^{-2}$	2400	2048
2D oblique ion firehose instability	$256(N_y=128)$	$256(L_y/d_i=128)$	1.0	$0.8\cdot10^{-2}$	400	256
	$N_y=128$	$L_y/d_i=128$				

Table II. Main numerical parameters for the the test problems. N_x is the number of grid points along the resolved direction, L_x is the simulation box length, Δx is the grid resolution, Δt is the time-step, T is the total simulation time and ppc are the number of particles per cell. We use $N_y = 4$ grid points in the transverse direction for all 1-D runs, while the grid size for the 2D firehose test problem is explicitly indicated. The ion Landau problem is unmagnetized, but we still use a reference magnetic field for calculating Ω_{ci}^{-1} and all the normalizations depending on it.

magnetic field fluctuations perpendicular to their propagation direction $\vec{k}$. Their dispersion relations are given by (see, e.g., Eq. 6.49-50 of Ref. 55)

$$\left(\frac{ck}{\omega}\right)^2 = 1 - \frac{\omega_{pe}^2}{\omega}\frac{1}{\omega \pm \Omega_{ce}} - \frac{\omega_{pi}^2}{\omega}\frac{1}{\omega \mp \Omega_{ci}}, \tag{24}$$

where the signs in the denominator of the first ($\pm$) and second term ($\mp$) of the right hand side correspond to L/R modes, respectively. Here, $\omega_{p\{e/i\}}$ are the electron/ion plasma frequencies and $\Omega_{c\{e/i\}}$ are the electron/ion cyclotron frequencies. In order to compare our results with the models used in the classical hybrid codes with massless electrons, we use the approximation of Eq. (24) for low frequencies and $m_e \to 0$:

$$(kd_i)^2 = \frac{(\omega/\Omega_{ci})^2}{1 \pm \omega/\Omega_{ci}}, \tag{25}$$

where the $\pm$ sign correspond to the R/L modes. We have used the relations $V_A = d_i\Omega_{ci}$ and $V_A/c = \Omega_{ci}/\omega_{pi}$, where V_A is the Alfvén speed and d_i is the ion skin depth.

In order to reproduce the theoretical curves given by the dispersion relation Eq. (24), we initialize a quasi-1D (mostly along one direction, averaging over 4 cells in the transverse direction) thermal plasma without any perturbation other than thermal noise, with

an external static magnetic field along the resolved $\hat{x}$-direction. The physical and numerical parameters for the simulation are summarized in Tables I and II, respectively. Note that $V_A/c = \Omega_{ci}/\omega_{pi}$ and $\sqrt{\beta_i} = \sqrt{2}v_{th,i}/V_A$, where $v_{th,i} = \sqrt{k_B T_i/m_i}$ is the ion thermal speed. The field output is written every 8 timesteps, resulting in a maximum frequency captured in the output of $\omega_{max}/\Omega_{ci} = \pi/(\Delta t \cdot 8 \cdot \Omega_{ci}) = 78.5$, a minimum resolved frequency of $\omega_{min}/\Omega_{ci} = 2\pi/(T\Omega_{ci}) = 0.0104$, and a maximum resolution in the parallel wave number of $k_{x,min}d_i = 0.06$. The timestep Δt and grid resolution Δx are chosen to satisfy a CFL number for the electron Alfvén speed of $V_{Ae}\Delta t/\Delta x = 0.5$. At the end of the simulation, the total energy is conserved within $1 \cdot 10^{-4}$ of its initial value.

The dispersion curves for the L and R modes can be obtained by a Fourier transform in space and time of the following complex combination of the components of the magnetic field.

$$\sqrt{2}B_{R/L} = B_y \pm iB_z \tag{26}$$

This choice corresponds to a change of basis vectors from Cartesian coordinates to vectors representing left- and right-handed circularly polarized waves (see Eq. 9.116 in Ref. 56 and Appendix B of Ref. 57). Thus, by plotting the spectral power in the magnetic field B_R in the $\omega - k$ space, we obtained the simulation dispersion-curves for the cases of zero (Fig. 3(a)) and finite electron mass (Fig. 3(b)). Our code reproduces correctly the cold full R-mode dispersion relation for both finite electrons mass (Eq. (24)) and massless electrons (Eq. (25)). Note that the latter dispersion curve is accurate for low frequencies, showing significant deviations from the cold full R-mode dispersion relation for $\omega \gg \Omega_{ci}$. This shows that our code can handle the cases of both zero and finite electron mass

Note that in Fig. (3) we did not show the higher frequency range close to the electron resonance $\Omega_{ce} = 100\,\Omega_{ci}$. This is because the available power in that region corresponding to higher k decays exponentially (plot not shown here). This observation agrees qualitatively with the known theoretical predictions of the electric field spectrum corresponding to the thermal fluctuations of a fully-kinetic plasma model[58,59].

Since the L mode tends asymptotically to the ion cyclotron frequency Ω_{ci} for large k, it is convenient to study its behavior in the low frequency range. The results for the inertial case (there are practically no differences with the inertia-less case in this frequency range), are shown in Fig. 4a). The agreement between the theoretical and simulation dispersion curves for the L mode (for $\omega > 0$) is quite good as long as it does not enter in to the triangular

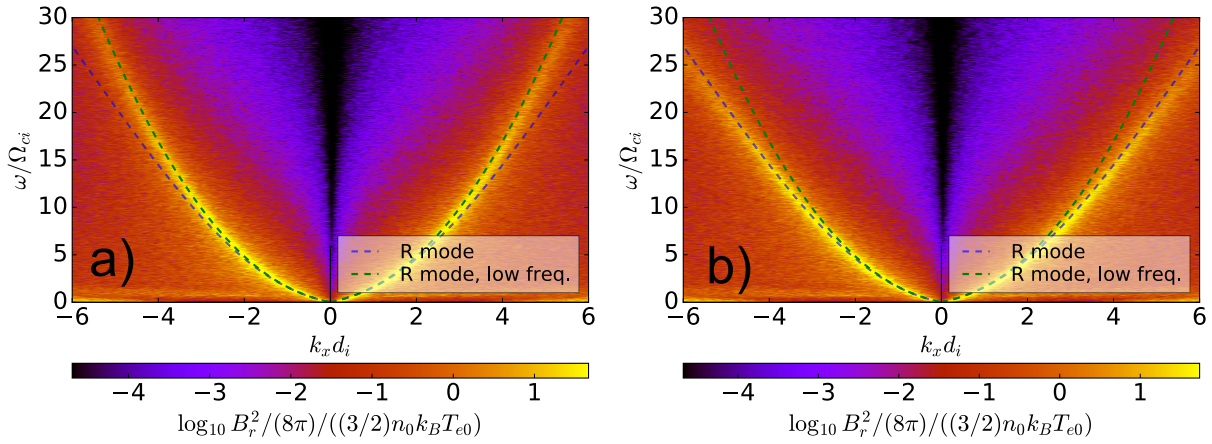

Figure 3. Right-handed (R) power spectra of perpendicular magnetic field for $B_y - iB_z$ a). inertialess case $m_e = 0$ and b) inertial case $m_e \neq 0$. Dashes lines are the cold plasma approximations discussed in the text.

regions approximately delimited by,

$$\omega = \Omega_{ci} \pm 3\, v_{th,i}\, k. \tag{27}$$

The frequency ω and wave number k satisfying this resonance condition represents thermal fluctuations caused by the ions. The "3" comes from the particles that are in the tail of the proton distribution function, three standard deviations from the mean (zero) velocity, since we started from normally distributed particles. The L modes gets heavily damped when it enters in this region, in agreement with the hot Vlasov dispersion relation (not shown here) and previous works[60].

Note that Fig. 4a) for $\omega < 0$ shows the right-handed polarized waves, since the polarization of the waves depends on the sign of ω[61]. For very low frequencies $\omega \ll \Omega_{ci}$, both L and R modes follows the (MHD) Alfvén wave dispersion relation $\omega = V_A\, k$. The deviations observed for high frequencies (for $kd_i \gtrsim 0.5$) are due to the Hall effect, i.e., when the electron and ion dynamics needs to be considered separately.

Fig. 4b) shows the same power spectra in B_R showed in Fig. 4a) from another simulation run enhancing thermal effects by setting $\beta_i = 0.1$, but otherwise exactly identical parameters. It shows the broadening of the triangular region due to the thermal fluctuations of ions in gyro-resonance, in agreement with Eq. (27) because the thermal speed is greater. Note that the distribution of spectral power in Fig. 4b) is more spread inside of this triangular-like

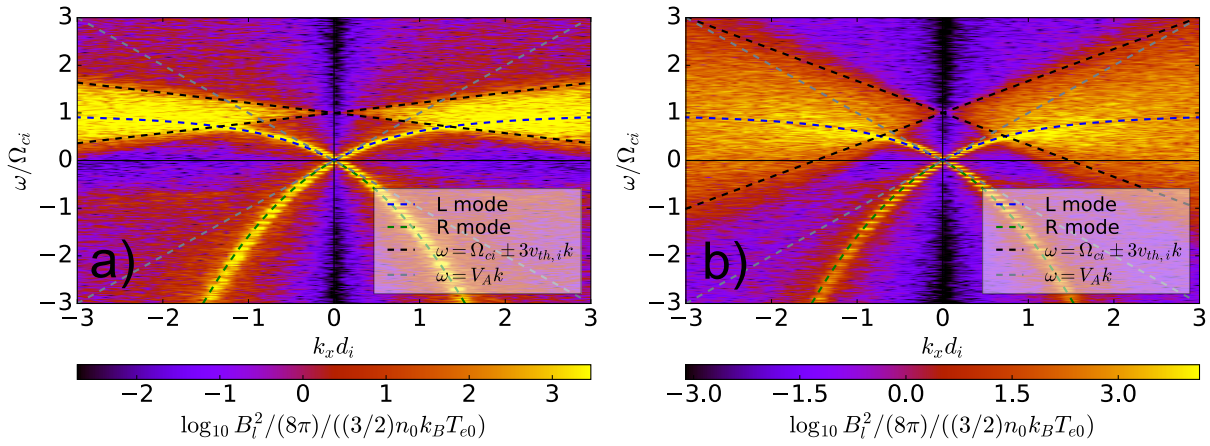

Figure 4. Left-handed (L) power spectra of perpendicular magnetic field $B_L = B_y - iB_z$ for a) $\beta_i = 0.01$ (standard parameters) and b) $\beta_i = 0.1$. Dashes lines are the cold plasma approximations discussed in the text. The curves with $\omega < 0$ correspond to right-handed polarized modes.

region compared to the previous lower-β_i case Fig. 4a).

B. Perpendicular propagation: ion Bernstein and X-mode

Bernstein waves are electrostatic plasma modes propagating nearly perpendicular to a magnetic field, coupled to gyrating particles[62]. They only exist in a plasma with finite temperature and have the remarkable property of being almost undamped and usually with a negative group velocity. Their dispersion curves are ordered in several bands at harmonics of the electron or ion cyclotron frequencies, with a general expression given by, e.g., Eq. 7.65 of Ref. 55. Because of the predicted high power at the harmonics of Ω_{ci}, ion Bernstein modes are ideal to test cyclotron resonances effect of perpendicularly propagating waves in our code. Since we are interested in the frequency range $\Omega_{ci} < \omega \lesssim \Omega_{ce}$, the corresponding waves are called pure ion Bernstein modes, with a contribution coming mostly from ion kinetic effects. The electrons contribute only with an additional term. The relevant dispersion relations is then (see., e.g., Eq. 69 in Ref. 63):

$$1 - \frac{\omega_{pe}^2}{\Omega_{ce}^2} - 2\omega_{pi}^2 \frac{e^{-\lambda_i}}{\lambda_i} \sum_{n=1}^{\infty} \frac{n^2}{\omega^2 - n^2\Omega_{ci}^2} I_n(\lambda_i) = 0. \tag{28}$$

where $I_n(\lambda_i)$ is the modified Bessel function (of the first kind) of order n and argument:

$$\lambda_i = k_\perp^2 \rho_i^2, \tag{29}$$

where $\rho_i^2 = v_{th,i}^2/\Omega_{ci}^2 = k_B T_i/(m_i \Omega_{ci}^2)$ is the thermal ion Larmor radius. Note that these waves are mostly independent of the electron temperature T_e. In the fluid limit $\lambda_i \to 0$, the upper bound in frequency tends to the lower hybrid oscillations $\omega = \Omega_{LH}$

In order to excite these waves, we initialize a quasi-1D thermal plasma along the $\hat{x}$ direction without any perturbation other than the thermal noise, and an initial external static magnetic field along the $\hat{z}$ direction (similar to the setup in Sec. IV A but changing the direction of the magnetic field). The physical and numerical simulation parameters are summarized in Table I and II, respectively. These parameters are a slightly different to the test problem in Sec. IV A, both plasma beta and mass ratio have been increased to discern more easily the thermal properties of the Bernstein modes depending on ρ_i, as well as to isolate the pure ion effects by choosing a larger separation of scales between electrons and ions. Note that the numerical parameters for this problem, combined to the output frequency (every 242 timesteps), results in a maximum captured frequency of $\omega_{max}/\Omega_{ci} = \pi/(\Delta t \cdot 8 \cdot \Omega_{ci}) = 31$, a minimum resolved frequency of $\omega_{min}/\Omega_{ci} = 2\pi/(T\Omega_{ci}) = 0.0104$, and a maximum resolution in the parallel wave number of $k_{x,min} d_i = 0.1$. The timestep Δt and grid resolution Δx have been chosen to give a CFL number for the electron Alfvén speed of $V_{Ae}\Delta t/\Delta x = 0.25$.

Fig. 5 shows the spectral power of the parallel electric field E_x. We can see a good agreement for all the harmonic of the fundamental mode $n = 1$ of the pure ion Bernstein waves. Note that all the modes start close to $(n+1)\Omega_{ci}$ for small $k_\perp$ and end up at $n\Omega_{ci}$ for large k, with a negative group speed asymptotically decreasing towards large k. We verified that smaller mass ratios produce additional gyro-resonances in thin bands at harmonics $n\,\Omega_{ci}$, on top of the pure ion Bernstein modes.[63]

In Fig. 5, we also show the theoretical cold dispersion relation for the X-mode (see, e.g., Eq. 6.59 in Ref. 55). This is a cold plasma mode with perpendicular propagation and several branches at differences frequencies. In our case of interest, with parameters suitable for the hybrid model, the maximum frequency of the X-mode is the lower-hybrid frequency. The small disagreement seen in Fig. 5 between the simulation results and the theoretical curve can be explained due to thermal effects neglected in the latter.

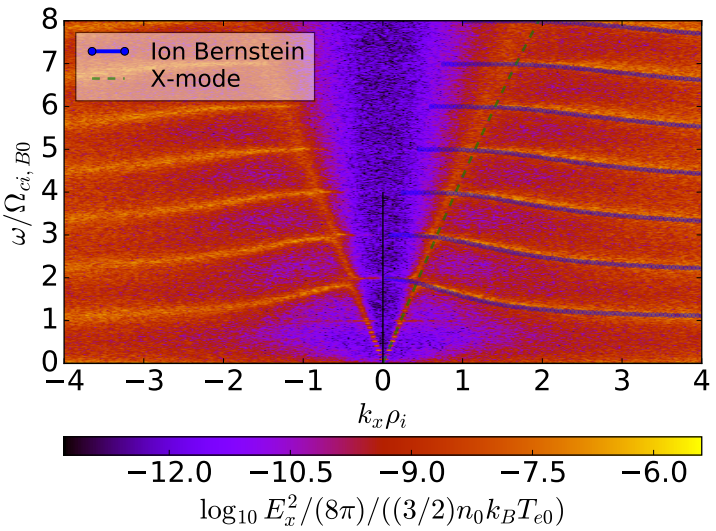

Figure 5. Power spectrum of the perpendicular electric field E_x. Theoretical curves for the ion Bernstein modes Eq. (28) and X-mode are shown in the right-half ($k > 0$) of this plot.

C. Ion beam R instability

A two ion component plasma is unstable to an instability driven by the relative drift speed between a main core ("c") ion population and a more tenuous beam ("b") component, along the direction of a background magnetic field. For a relatively cold ion beam, the instability with lowest threshold produces unstable magnetosonic waves with right-handed polarization (see, e.g., Refs. 61, 64, and 65). There are two different types of this instability: resonant and non-resonant. In the first one, the ions produce waves with phase speeds resonating in the tail of the ion thermal distribution. The second one is fluid-like, driven by the bulk anisotropy of the ion distribution, and therefore much stronger than the resonant-one, because most of the particles contributes to the interaction.

Case	n_b/n_e	U_{b-c}/V_A	$\beta_c = \beta_b$	T_c/T_b	T_b/T_e	ppc-beam
Resonant R-beam	0.02	10	1.0	1	1	512
Non resonant R-beam	0.1	10	1.0	1	1	512

Table III. Main physical and numerical parameters for ion beam R instability. c/b stand for beam/core related quantities. n is density, U_{b-c} is the relative beam-code drift speed.

In order to trigger this instability, we consider a quasi-1D thermal plasma without any perturbation other than the thermal noise, and an external static magnetic field along the $\hat{x}$ direction. We consider two populations of ions: the main core and a tenuous beam. The specific parameters of those two populations are summarized in Table III for the two cases to be considered. The remaining parameters referred only to the "core"-ions (and electrons) are specified in Table I and II. The CFL number for the electron Alfvén speed is $V_{Ae}\Delta t/\Delta x = 0.4$. Note that we chose only half of the number of particles per cell for the beam compared to the core, changing suitably its macrofactor (ratio of physical to numerical particles) to compensate for its lower density. We perform the simulation in the reference frame of the center of mass of the ions, satisfying:

$$n_b\vec{U}_b + n_c\vec{U}_c = 0 \tag{30}$$

where $n_{(b/c)}$ and $\vec{U}_{(b/c)}$ are the densities and bulk drift speeds of the beam/core population in this reference frame, respectively. Eq. (30) leads to the explicit initial drift speeds of each species in term of their relative drift $\vec{U}_{b-c} = \vec{U}_b - \vec{U}_c$:

$$\vec{U}_b = \frac{1}{1+n_b/n_c}\vec{U}_{b-c}, \tag{31}$$

$$\vec{U}_c = -\frac{n_b/n_c}{1+n_b/n_c}U_{b-c}. \tag{32}$$

Note that in this reference frame the total ion current also vanishes.

Fig. 6 shows the energies of the beam and core components for the resonant case. The green curve in Fig. 6(b) shows the increase of the magnetic field energy due to the development of the instability. We can see in Fig. 6a) that the parallel beam drift speed diminishes very quickly during the linear growth phase of the instability, and at the same time the perpendicular energy rises. This corresponds mostly to perpendicular beam heating due to the waves generated by the instability. Fig. 6b) shows that the parallel core energy (consisting of field aligned thermal energy and the parallel bulk drift speed with respect to the center of mass) is mostly unaffected, while the core is heated in the perpendicular direction due to a mechanism similar to that of the beam. Our results agree with the ones shown in Fig. 4 of Ref. 31 and Fig. 8 of Ref. 64.

In order to compare with the predictions of linear theory[64,65], we calculate the three most unstable Fourier modes of the magnetic field component B_y. The results for the resonant case are shown in Fig. 7. We determine the linear growth rate of those modes via a linear

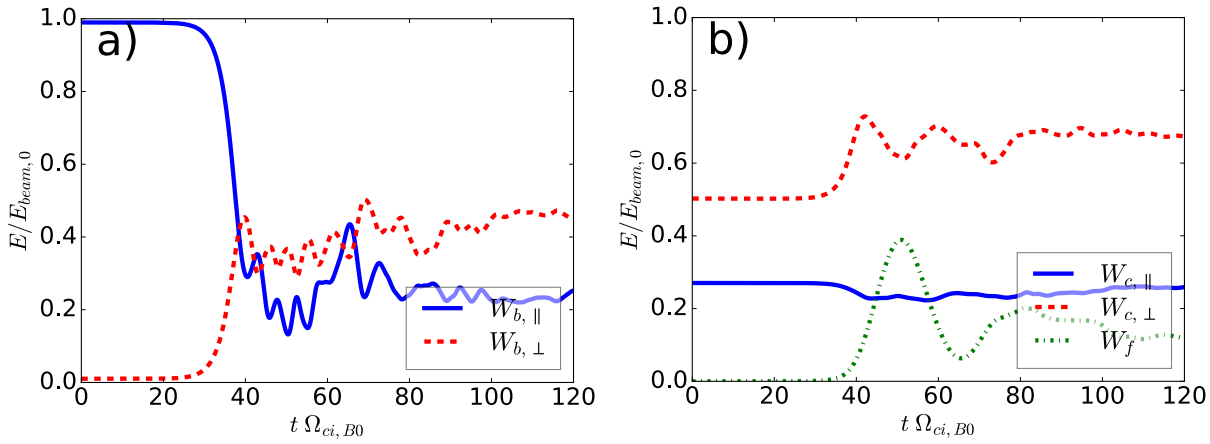

Figure 6. Time histories of total particle energies for both beam and core. Resonant case. a) Beam particle parallel energy $W_{b,\parallel}$ and perpendicular energy $W_{b,\perp}$. b) Core particle parallel $W_{c,\parallel}$, perpendicular energy $W_{c,\perp}$ and magnetic field energy W_f.

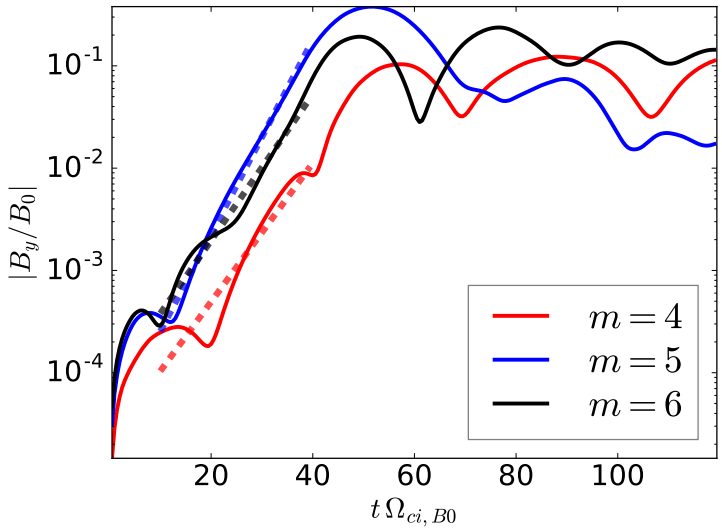

Figure 7. Time history of the Fourier modes 4-6 of $B_y(k_x)$ for the resonant case. The dashed lines represent the linear fitting used to calculate the growth rate γ shown in Fig. 9(a).

fitting during the linear state, indicated by dashed lines in Fig. 7. Fig. 9(a) shows the growth rates γ of these and all the other unstable modes vs wave number k. In fig. 9(a) we also plot the theoretical growth rates obtained by solving the hot Vlasov dispersion relation[64,65], illustrating very clearly the good agreement with our results.

The stack plot of B_y in Fig. 8a) confirms that, during the linear phase, there is a clear

dominant mode with five full wavelengths in the simulation box. This plot also shows the preferentially forward propagating waves (to the right), as expected from the linear theory.

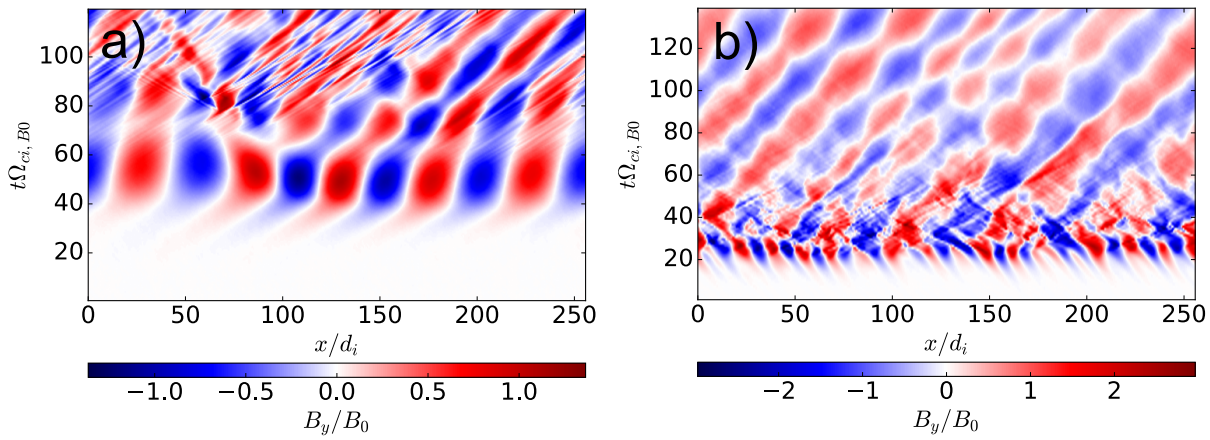

Figure 8. Stack time plot evolution of B_y. a) Resonant case. b) Non-resonant case

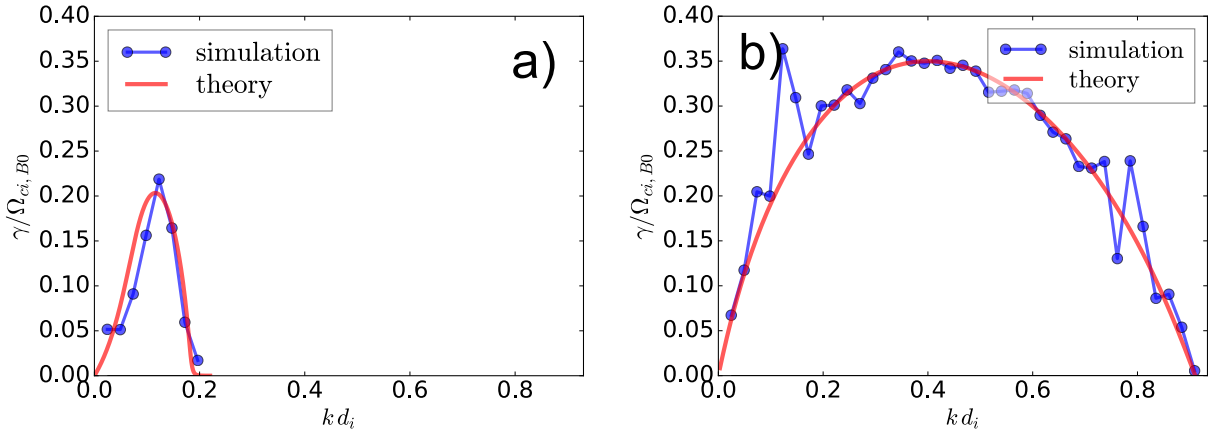

Figure 9. Growth rates γ vs k for the Fourier components of B_y. a) Resonant case. b) Non-resonant case. The theoretical curve was obtained by solving the hot plasma dispersion relation corresponding to these parameters.

The dominant oscillation with five full wavelengths also affects both core and beam population. This can be seen in the corresponding phases spaces $x - v_y$ (perpendicular velocity) shown in Fig. 10. Note the much stronger spreading of the beam population compared to the core. A significant number of beam particles reach perpendicular speeds close to $7V_A$, just below the initial (parallel) drift speed ($10V_A$). This is qualitatively in agreement with previously published results (see, e.g., Fig. 5 of 64, Fig. 3 of 31).

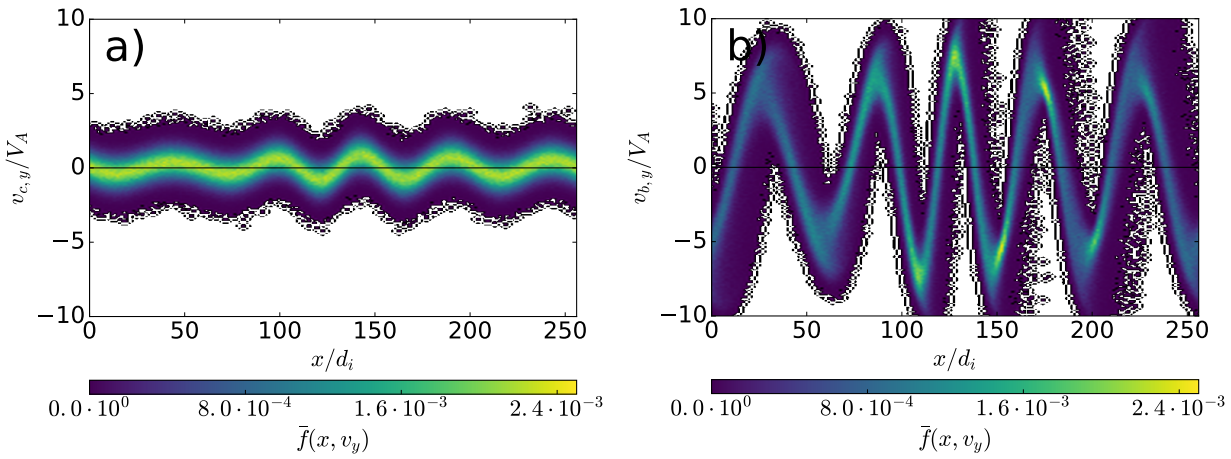

Figure 10. Ion core (a) and beam (b) phase space $x - v_y$, at $t\Omega_{ci} = 40$. Resonant case. The normalized distribution function $\bar{f}$ is shown, satisfying $\iint f \, d\vec{x} \, d\vec{v} = 1$.

The results for the stronger, fluid-like, non-resonant case also match with the linear theory, as seen in Fig. 9(b). This plot shows the growth rate of the first 38 Fourier modes of B_y, up to the maximum unstable wave number predicted by the theory ($kd_i \approx 1$). In Fig. 8(b) we can also see the evolution of the spatial structure of B_y, showing much smaller wavelengths at maximum growth rates than in the resonant case. Note that the modes propagate to the left (backward waves) during the initial linear phase, also in agreement with the predictions of linear theory. Only much later, after saturation, the dominant modes propagate forward (to the right). Overall, the amplitude of these modes is much larger than in the resonant-case, as expected from a stronger instability.

D. Ion Landau damping

One of the most characteristic kinetic plasma processes is the Landau damping[66], where an electrostatic wave (from the ion-acoustic branch) is damped by transferring its energy to particles satisfying the resonance condition $\omega = v_{\parallel} k$. Close to the ion frequencies Ω_{ci} and length scales d_i, this process can be observed for long wavelengths $k\lambda_{De} \ll 1$ and for the range of phase speeds $v_{th,i} < v_\phi < v_{th,e}$, because this implies a weak damping in the regime $T_e \gg T_i$. This is equivalent to $|\xi_i| \gtrsim 1$ for the (cold) ions and $|\xi_e| \ll 1$ for the (hot) electrons,

where

$$\xi_{(i,e)} = \frac{\omega}{k\sqrt{2}v_{th,i}} = \frac{\omega_r + i\gamma}{k\sqrt{2}v_{th,(i/e)}}. \tag{33}$$

The hot dispersion relation that describes accurately the ion-acoustic waves, subject to ion Landau damping, in the hybrid approximation, is given by[67]:

$$Z'(\xi_i) = -2\frac{T_i}{T_e}. \tag{34}$$

where Z' is the derivative of the plasma zeta function[68]:

$$Z(\xi_i) = \frac{1}{\sqrt{\pi}} \int_{-\infty}^{\infty} \frac{\exp(-x^2)}{x - \xi_i} dx, \qquad \mathfrak{Im}(\xi_i) > 0. \tag{35}$$

In order to show this process with our hybrid code, we setup a quasi-1D electrostatic simulation (no initial magnetic field) along the $\hat{x}$ direction, with a density perturbation of the form:

$$n(x) = n_0(1 + \epsilon\cos(k_m x)), \qquad k_m = \frac{2\pi m}{L_x}. \tag{36}$$

where L_x is the simulation length box and m the excited mode number. The parameters specific of this test problem are given in Table IV while the remaining physical and numerical parameters are in Table I and Table II.

Case	ϵ	m
ion Landau damping	0.03	4

Table IV. Main numerical parameters for the ion Landau damping test problem. We vary the ratio T_i/T_e by changing T_e and always keeping T_i fixed.

The results of this test problem are summarized in Fig. 11. The left panel shows the time evolution of the Fourier modes number $m = 4$ of the electrostatic field E_x. We can see very clearly that by decreasing the temperature ratio T_i/T_e the damping becomes weaker, and the initially imposed wave can propagate longer (without losing power). This is in agreement with the theoretical expression Eq. (34). Fig. 11(a) also shows the damping rate calculated with a exponential fitting during the linear stage of the process, until the power of the initial wave reaches the noise floor. The growth rates are plotted against the temperature ratio

T_i/T_e in Fig. 11(b) as red diamonds. The theoretical approximation for the damping rates, Eq. (34), is plotted as a blue curve. The agreement with the theory is very good, even considering that our code uses a full PiC approach for the ions, different from less noisy approaches such as hybrid-Vlasov codes[21], δf-hybrid PiC codes[67] or pure Eulerian Vlasov codes.[69]

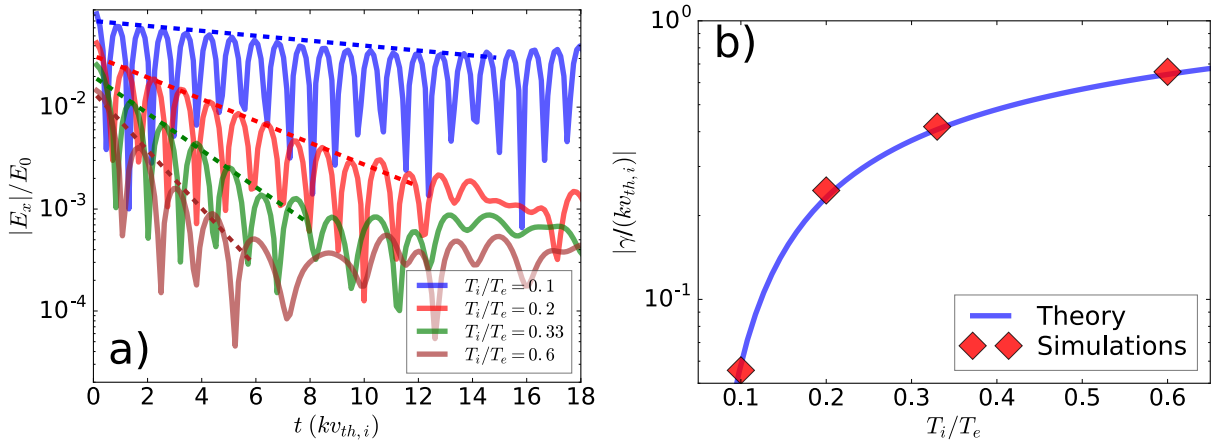

Figure 11. Landau damping test problem. Time evolution (a) and comparison of the theoretical and simulation growth rates (b) of the Fourier modes $m = 4$ for the electrostatic field E_x and different temperature ratios T_i/T_e. In a), the dashes lines are the exponential fits from which the damping rates were calculated.

It is important to mention that simulations with a hybrid PiC code in the regime $T_e \gg T_i$ are prone to a numerical instability and/or heating. As found by Refs. 70 and 71, the regime of high electron temperature might excite a finite grid instability analogous to the well known in fully-kinetic PiC codes[1]. In the latter case, the finite grid instability is due to the interaction of plasma oscillations (Langmuir waves) with the aliases of the spatial grid whenever the grid cell size is much larger (within a factor of 2-3) than the Debye length. The typical growth rates are on the order of the plasma frequency, with the electrons being heated until the electron temperature reaches a value such as the Debye length becomes on the order of the grid cell size. Similarly, in hybrid-PIC codes, the finite grid instability is due to ion-acoustic waves whenever the temperature ratio $T_e/T_i \gg 1$ (no sharp threshold), making difficult to choose parameters (in this regime) that make a simulation stable within a reasonable computational cost. This instability heats ions up to the ion thermal speed becomes comparable to the ion acoustic speed (and therefore, $T_e/T_i \sim 1$). Refs. 70 and

71 found that even though the instability threshold is not crossed, there will always be a numerical heating in the regime $T_e/T_i > 1$. Smoothing and use of higher order particle shape functions helps to keep this effect efficiently controlled, and to a much smaller extent the increase of macro-particles per cell. This is the reason to not simulate scenarios with even higher electron temperature than the case $T_e/T_i = 10$ shown in Fig. 11.

E. Firehose instability

Temperature anisotropy can be a source of free energy for instabilities. In the hybrid regime, for a sufficiently large plasma-β_i and for $T_{i,\parallel} > T_{i,\perp}$, the corresponding fastest growing instability is called firehose (see, e.g., Sec. 3.4 of Ref. 72). Although it is possible to describe this instability in an (anisotropic) MHD or two-fluid model, its growth rate and maximum wave number when propagating obliquely to a magnetic field is correctly reproduced only when considering ion kinetics, in particular finite Larmor radius effects[73].

Case	$\beta_{i,\perp} = \beta_i$	$\beta_\parallel$
ion firehose instability	$300/\pi$	$3+\beta_{i,\perp}$

Table V. Main physical parameters for the ion firehose test problem.

We reproduce this instability with our code by initializing a quasi-1D simulation of a high beta plasma, with the external static magnetic field along the $\hat{x}-$direction. The specific parameters are given in Table V while the remaining physical and numerical parameters are in Table I and Table II.

Our results are summarized in Fig. 13. The left panel shows that the initially higher values of the parallel ion temperature (proportional to $v^2_{th,i,x}$) decrease in time reaching similar values to those of the perpendicular ion temperature (associated with $v^2_{th,i,y}$ or $v^2_{th,i,z}$). In this way, the source of free energy of the instability is exhausted. This instability produce transverse magnetic fluctuations during its linear stage, whose first three Fourier modes are shown in Fig. 13(b). According to linear theory[67], the most unstable mode should $m = 1$ with $\gamma = 0.011\Omega_{ci}$, and similarly for the real frequency ω (both positive and negative). This solution of the dispersion relation for both γ and ω relation is plotted in Fig. 12 where we also indicate the mode number 1 in our configuration. This clearly shows that our setup al-

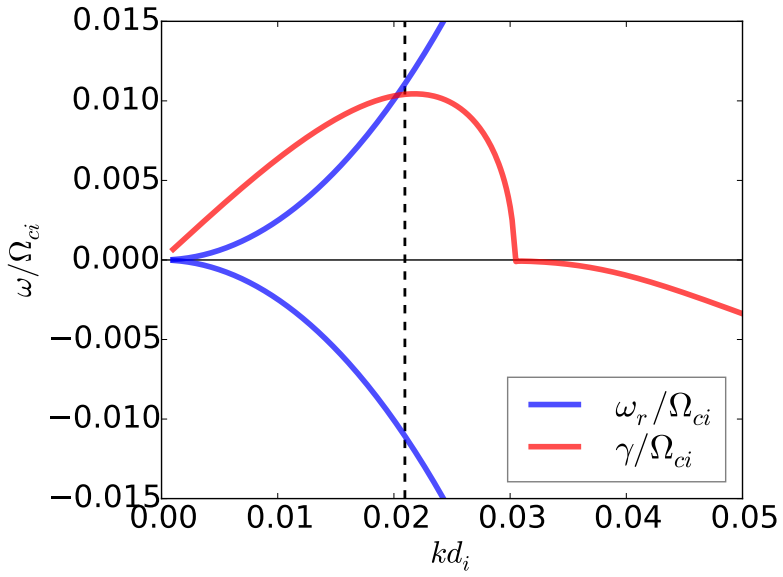

Figure 12. Frequency and growth rate of the hot plasma dispersion relation for the firehose parameters. The black vertical dashed line represents the wave number k associated to the mode $m = 1$.

lows to develop only a single mode, because all the harmonics that our simulation box allows are damped. Note that the real frequency curve have both positive and negative branches, indicating that the instability generates a superposition of both forward and backward propagating waves. Fig. 13(b) shows this fact and also that the theoretical γ fits very well with the growth rate of this instability.

F. Oblique (2D) firehose instability

Ion temperature anisotropies with $T_{i,\parallel} > T_{i,\perp}$ can also drive (firehose) instabilities with waves propagating obliquely to a background magnetic field (AF, oblique propagating Alfvén firehose). In a 2D geometry and under suitable parameters, both (firehose) instabilities with waves propagating obliquely and parallel to the magnetic field (see Sec. IV E, denoted onwards as WF: parallel propagating Whistler-firehose,) can coexist with similar growth rates. The oblique firehose instability was found for the first time by Ref. 74 and simulated together with the parallel firehose by Ref. 75. Different from the parallel propagating firehose known since much earlier, the oblique firehose instability generates waves with zero frequency that can isotropize more efficiently the ion temperature anisotropy.

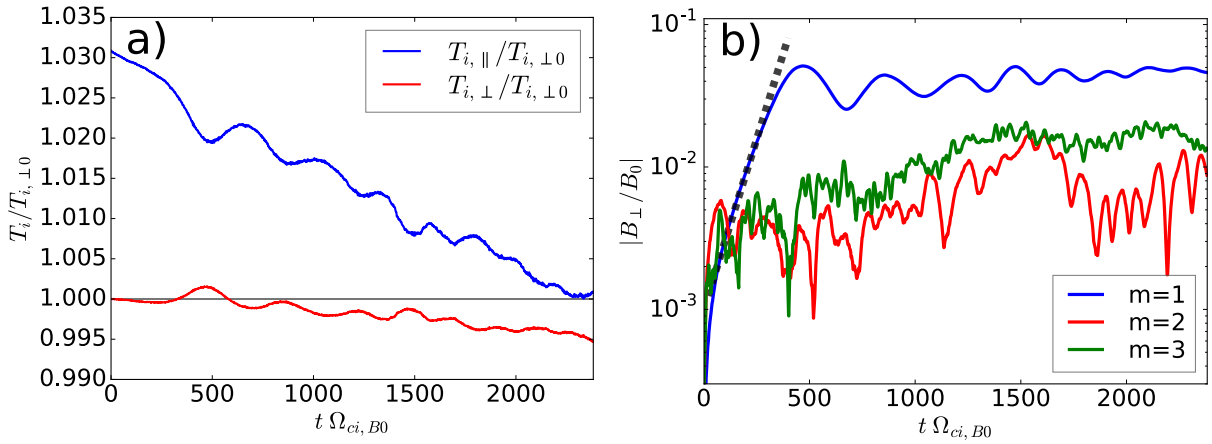

Figure 13. Time evolution of quantities related with the firehose instability test problem. a) Components of the globally averaged thermal ion speed: $v^2_{th,i,\alpha} = (1/N)\sum_j^N (v_{\alpha,j} - V_\alpha)^2$, with the component $\alpha = x, y, z$ for the jth ion of a total of N and V_α is the $\alpha-$component of the bulk (average) ion speed. b) Fourier modes of the transverse magnetic field $B_\perp(k_x) = \sqrt{[B_y(k_x)]^2 + [B_z(k_x)]^2}$.

In this section, we are going to show a 2D test problem showing the simultaneous existence of this kind of instabilities and their identification based on their different properties, following Ref. 74. By comparing with the linear and non-linear theory, this will allow us to prove that our code can handle the spectral transfer of power between waves with different propagation angles and the cyclotron resonances effects on the ion distribution function. We reproduce this instability with our code by initializing a 2D simulation with the external static magnetic field along the $\hat{x}-$direction. The specific parameters are given in Table V while the remaining physical and numerical parameters are in Table I and Table II. These parameters give a comparable maximum growth rate of $\gamma/\Omega_{ci} \sim 0.056$ for the parallel firehose instability (AF) and $\gamma/\Omega_{ci} \sim 0.059$ for the perpendicular firehose instability (WF)[75].

Case	$T_{i,\perp}/T_{i,\parallel}$
2D ion firehose instability(ies)	0.4

Table VI. Main physical parameters for the ion firehose test problem.

Our results are summarized in Fig. 14 with the time evolution of two quantities character-

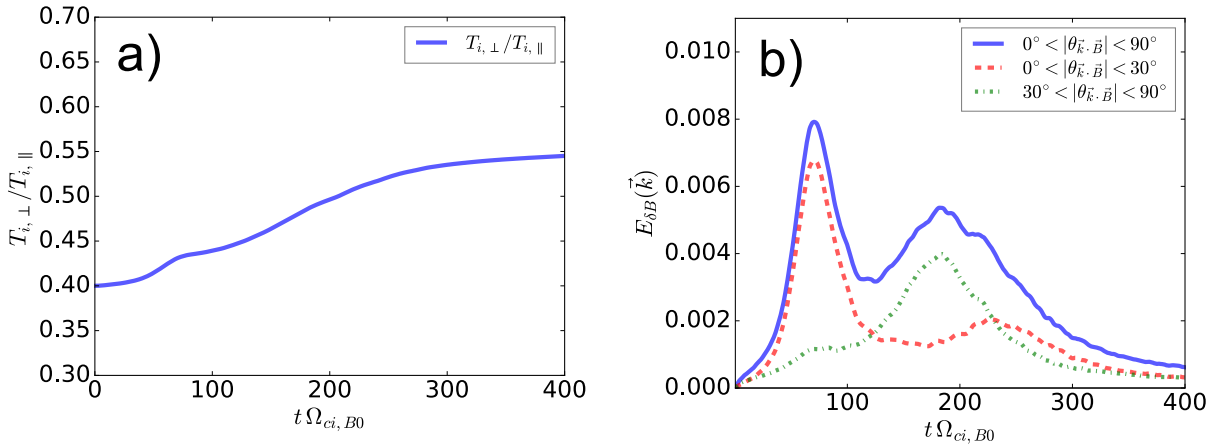

Figure 14. Time evolution of the firehose 2D test problem. a) Ion anisotropy $T_{i,\perp}/T_{i,\parallel}$. b) Spectral power of the total magnetic field fluctuating energy $E_{\delta B}$ and its components: near parallel propagation ($0° < \theta_{\vec{k}\cdot\vec{B}} < 30°$) and oblique propagation ($60° < \theta_{\vec{k}\cdot\vec{B}} < 90°$)).

izing the system. Fig. 14a) shows the drop in the initial imposed ion temperature anisotropy (globally averaged), exhausting the source of free energy of the firehose instability(ies). Most of the anisotropy is reduced in the time interval between $100 < t\Omega_{ci} < 200$, to later remain practically constant. This origin of this behaviour is clearly explained in Fig. 14b) with the time evolution of the spectral power in the total magnetic field fluctuating energy $E_{\delta B}(\vec{k})$ and its components aligned and oblique to the background magnetic field. This splitting requires to define the angle in the Fourier space $\theta_{\vec{k}\cdot\vec{B}} = \mathrm{acos}(k_x/\sqrt{k_x^2 + k_y^2})$ between the wave number $\vec{k}$ vector and and the background magnetic field in x. The power in a given interval of angles is obtained then just by integrating all the power in δB^2 which falls into that range. In this way, Fig. 14b) shows that most of the magnetic fluctuations are initially propagating nearly parallel to the magnetic field. These fluctuations, reaching a peak near $t\Omega_{ci} \sim 100$, are due to the parallel propagating firehose instability. Later, between $100 \lesssim t\Omega_{ci} \lesssim 200$, the power in the parallel fluctuations drops considerably while the nearly oblique waves start to develop, contributing with most of the power in the energy near $t\Omega_{ci} \sim 200$. Later, until the end of the simulation at $t\Omega_{ci} \sim 400$, the power in both parallel and oblique propagating waves decreases considerably. All these features match very closely with the results published in Ref. 74 and are explained to a greater extent there.

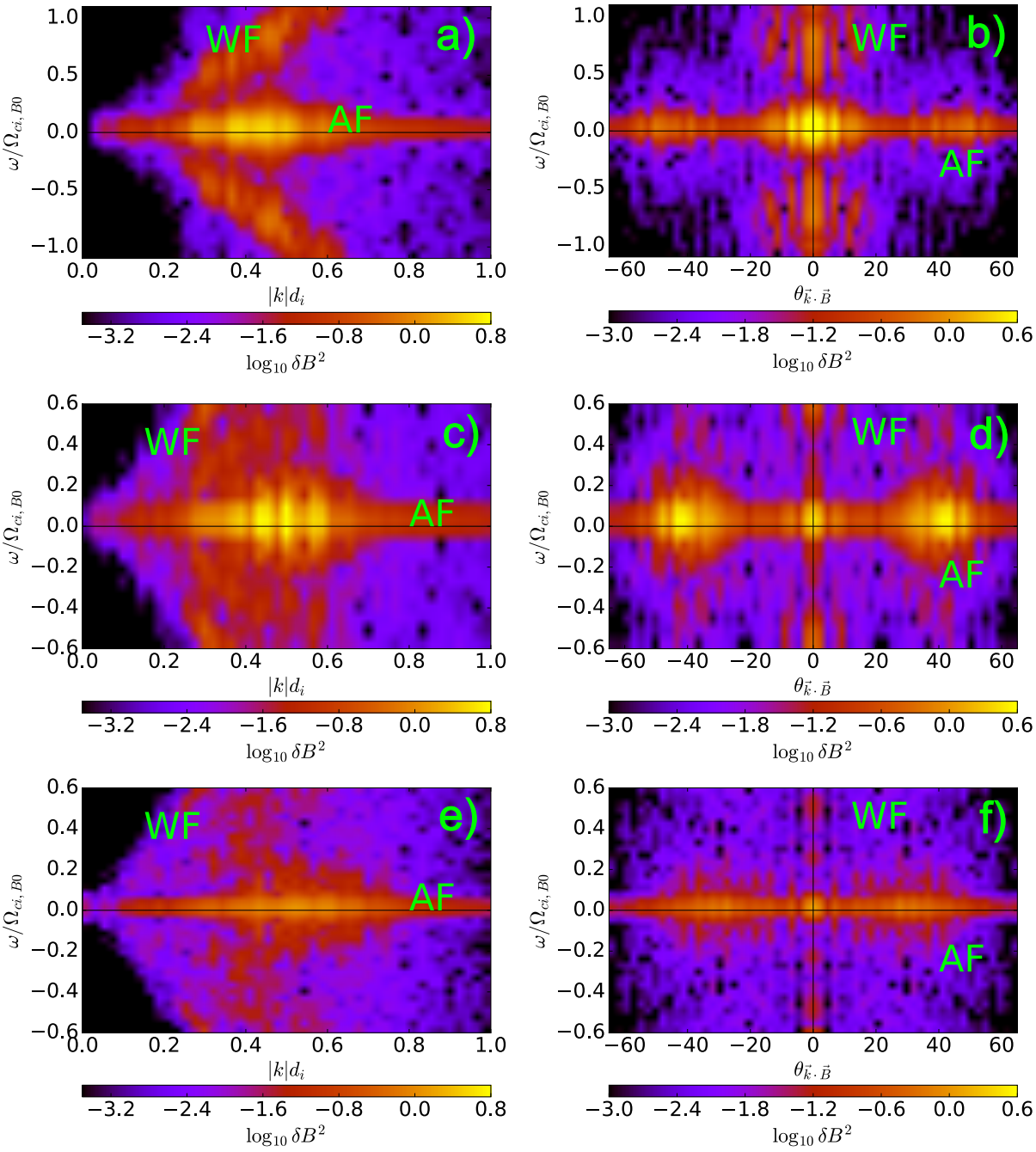

Figure 15. Dispersion relations of the power in the magnetic field fluctuating energy of the firehose 2D test problem. Left: $\omega - |k|$. Right: $\omega - \theta_{\vec{k}\cdot\vec{B}}$. First row: initial, between $0 < t\Omega_{ci} < 100$. Second row: middle, between $100 < t\Omega_{ci} < 200$. Third row, later, $200 < t\Omega_{ci} < 400$. WF stands for the parallel propagating Whistler-firehose, while AF stands for oblique propagating Alfvén firehose.

Fig. 15 shows the distribution of spectral power in the $\omega - |k|$ (left column) and $\omega - \theta_{\vec{k}\cdot\vec{B}}$

(right column) planes for the different phases of spectral power transfer between parallel and oblique waves identified before. For early times $0 < t\Omega_{ci} < 100$, Fig. 15(b) shows the power in the parallel propagating firehose (WF) at $\theta_{\vec{k}\cdot\vec{B}} \sim 0$ and with a frequency near $\omega \sim \pm 0.6$. This branch follows the whistler R Alfvén mode with finite phase speed as seen in Fig. 15(a) near $|k|d_i \sim 0.6$. On the other hand, the oblique waves generated by the oblique Alfvén firehose instability (AF) are seen at $\theta_{\vec{k}\cdot\vec{B}} \sim 45$ in Fig. 15(b), at nearly zero frequency, and with a similar wave number as for the parallel propagating WF. There is also power at $\theta_{\vec{k}\cdot\vec{B}} \sim 0$ and with $|k|d_i \sim 0.6$. All these features agree very well with the solutions of the Vlasov dispersion relation for these parameters (see Figs. 2 and 4 in Ref. 75).

Later, between $100 < t\Omega_{ci} < 200$, Fig. 15(d) shows that power is transferred to the oblique waves of the AF instability as evidenced by an enhancement of power there and a decrease in the WF branch after its saturation. This is consistent with the behavior seen in Fig. 14b). Finally, between $200 \lesssim t\Omega_{ci} \lesssim 400$, after the saturation of the AF instability, Fig. 15f) shows very little power in both AF and WF branches (in particular the latter one), as a result of the exhaustion of the ion anisotropy which drives these instabilities.

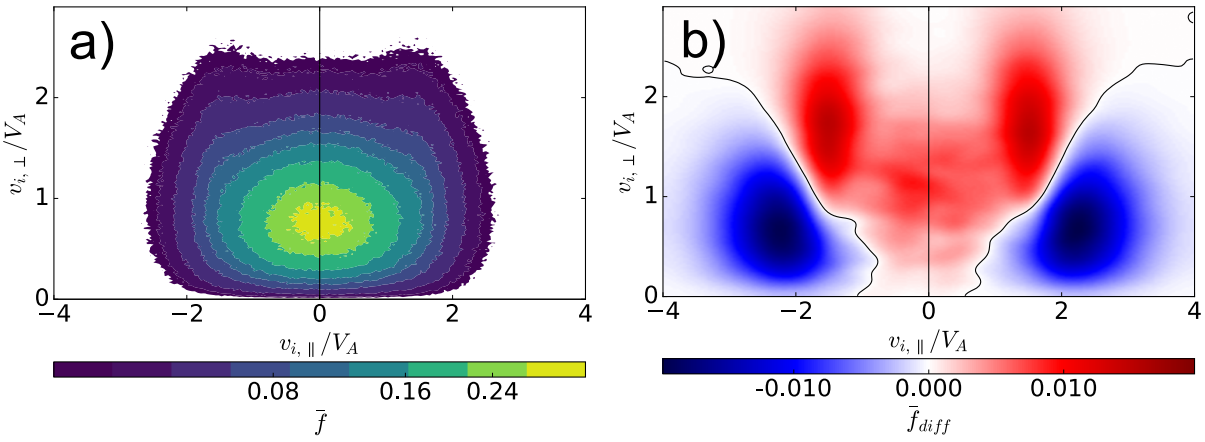

Figure 16. Ion VDF of the firehose 2D test problem in the $v_\perp - v_\parallel$ plane. a) Final VDF at $t\Omega_{ci} = 400$ b) Difference between the final and initial VDFs. The black line represents the contour level with no changes.

Fig. 16 shows the effects on the ion velocity distribution function (VDF) of the different wave activity generated by the two firehose instabilities. In particular, Fig. 16a) shows the final ion VDF at $t\Omega_{ci} = 400$ with two peaks at $v_\perp/V_A \sim 2$ and $|v_\parallel|/V_A \sim 1$. The origin of these non-Maxwellian features can be traced back in Fig. 16b), which shows the difference

between the final and initial VDFs. There is an increase in the number of particles (red contours) precisely in the velocity space region mentioned before with the non-Maxwellian features between $v_\perp/V_A \sim 2$ and $|v_\parallel|/V_A \sim 1$. These particles come from the region where there is a decrease (blue contours) near $v_\perp/V_A \sim 0.5-1$ and $|v_\parallel|/V_A \sim 2$. This is evidence that these particles were accelerated in the perpendicular direction via cyclotron resonance $\omega = k_\parallel v_{\parallel,res} \pm \Omega_{ci}$, a well known effect of the damped waves via the AF instability. Indeed, as shown previously, this instability is characterized for waves with $\omega \sim 0 \ll \Omega_{ci}$. Then, for $k_\parallel d_i = 0.5-0.7$ (see Fig. 15(d)), the resonant phase speed can be estimated to be in $v_{\parallel,res} \sim 1.4-2V_A$, in agreement with the modified regions in the velocity space $v_\parallel$ in Fig. 16b). Note that this cyclotron resonant effect does not happen in the first stage of the evolution of the system dominated by the WF instability, because their unstable waves do not satisfy the resonant condition.

V. CONCLUSION

We presented a new hybrid code with kinetic ions modeled with the PiC method and inertial electrons modelled with an EMHD approach. Our code was validated through a set of six different test problems, covering different aspects of the kinetic ion dynamics and electron inertia.

1) Parallel electromagnetic and 2) perpendicular electrostatic modes with the purpose of checking the excitation of normal plasma modes arising from thermal noise. We reproduce that the R mode and the ion Bernstein modes are mostly undamped, while the L mode gets damped when entering the dispersive regime for $k > d_i$ in the low frequency regime ($\omega < \Omega_{ci}$). The L mode and ion Bernstein modes follow the correct dispersion curves with practically pure ion contribution. The R mode has the correct contribution from both kinetic ions and inertial electrons, especially significant in the high frequency regime $\omega \gg \Omega_{ci}$. The latter is because it differs by a large amount from the curve followed by the model with kinetic ions and massless electrons, which is also contained in the code as a limiting case.

3) Ion beam R instability to check that the code reproduce correctly the evolution of instabilities having a relative drift speed between two ion populations as its source of free energy, and correctly handling multiple ion species in general.

4) Ion Landau damping to prove that the code can reproduce correctly the damping of

electrostatic waves via wave-particle interactions.

5) Ion firehose instability to check the correct development of instabilities with ion temperature anisotropy as their source of free energy.

6) 2D oblique ion firehose instability to check the simultaneous presence of instabilities with waves propagating at different angles with respect to the background magnetic field in a 2D geometry. This also allows to verify the expected power transfer between these waves during the non-linear stage of these instabilities, in addition to verify perpendicular ion acceleration due to ion cyclotron resonance.

Altogether, these tests show that our simulation code can reproduce correctly the relevant ion kinetic physics in the regime $\omega \sim \Omega_{ci}$ and $k \sim d_i^{-1}$, by comparing with the predictions of linear (and non-linear) theory. Our hybrid code does no approximations for the electron inertial contributions appropriate for $\omega \sim \Omega_{ce}$ and $k \sim d_e^{-1}$, other than the equation of state relating electron pressure and temperature. Therefore, the presented simulation approach is ideal to study dissipative or multi scale phenomena between electron and ion scales, like magnetic reconnection and turbulence in laboratory, space, and astrophysical plasmas.

ACKNOWLEDGMENTS

We acknowledge the developers of the ACRONYM code (Verein zur Förderung kinetischer Plasmasimulationen e.V.) which was used as part of our hybrid code. P.M. and J.B. acknowledge the financial support by the Max-Planck-Princeton Center for Plasma Physics. P.K. acknowledges support from the NRF and DST of South Africa through the following disclosure:
This work is based upon research supported by the National Research Foundation and Department of Science and Technology. Any opinion, findings and conclusions or recommendations expressed in this material are those of the authors and therefore the NRF and DST do not accept any liability in regard thereto.

REFERENCES

[1]C. Birdsall and A. B. Langdon, *Plasma Physics via Computer Simulation* (IOP Publishing, Bristol, England, 1991).

[2]R. W. Hockney and J. Eastwood, *Computer Simulation Using Particles* (IOP Publishing, 1988).

[3]J. Büchner, C. Dum, and M. Scholer, *Space Plasma Simulation* (Springer-Verlag, Berlin Heidelberg, 2003).

[4]A. Mangeney, F. Califano, C. Cavazzoni, and P. Travnicek, "A Numerical Scheme for the Integration of the Vlasov-Maxwell System of Equations," J. Comput. Phys. **179**, 495–538 (2002).

[5]T. Umeda, "Simulation of Collisionless Plasma With the Vlasov Method," in *Comput. Phys. Commun.*, edited by B. S. Doherty and A. N. Molloy (Nova Science Publishers, 2012) Chap. 5, pp. 315–332.

[6]S. V. Bulanov, F. Pegoraro, and A. S. Sakharov, "Magnetic reconnection in electron magnetohydrodynamics," Phys. Fluids B Plasma Phys. **4**, 2499 (1992).

[7]N. Jain, A. Das, P. Kaw, and S. Sengupta, "Nonlinear electron magnetohydrodynamic simulations of sausage-like instability of current channels," Phys. Plasmas **10**, 29 (2003).

[8]D. Winske, L. Yin, N. Omidi, H. Karimabadi, and K. Quest, "Hybrid Simulation Codes: Past, Present and Future-A Tutorial," in *Space Plasma Simulation* (Springer Berlin Heidelberg, Berlin, Heidelberg, 2003) pp. 136–165.

[9]A. S. Lipatov, *The Hybrid Multiscale Simulation Technology* (Springer-Verlag, Berlin Heidelberg, 2002).

[10]M. A. Shay, J. F. Drake, R. E. Denton, and D. Biskamp, "Structure of the dissipation region during collisionless magnetic reconnection," J. Geophys. Res. **103**, 9165 (1998).

[11]M. Hesse, D. Winske, and M. M. Kuznetsova, "Hybrid modeling of collisionless reconnection in two-dimensional current sheets: Simulations," J. Geophys. Res. Space Phys. **100**, 21815–21825 (1995).

[12]D. W. Forslund and J. P. Freidberg, "Theory of Laminar Collisionless Shocks," Phys. Rev. Lett. **27**, 1189–1192 (1971).

[13]D. Hewett and C. Nielson, "A multidimensional quasineutral plasma simulation model," J. Comput. Phys. **29**, 219–236 (1978).

[14]D. Eremin, T. Hemke, and T. Mussenbrock, "A new hybrid scheme for simulations of highly collisional RF-driven plasmas," Plasma Sources Sci. Technol. **25**, 015009 (2016).

[15]D. W. Swift, "Use of a Hybrid Code for Global-Scale Plasma Simulation," J. Comput. Phys. **126**, 109–121 (1996).

[16]D. W. Swift and Y. Lin, "Substorm onset viewed by a two-dimensional, global-scale hybrid code," J. Atmos. Solar-Terrestrial Phys. **63**, 683–704 (2001).

[17]M. M. Kuznetsova, M. Hesse, and D. Winske, "Kinetic quasi-viscous and bulk flow inertia effects in collisionless magnetotail reconnection," J. Geophys. Res. **103**, 199 (1998).

[18]M. A. Shay, J. F. Drake, B. N. Rogers, and R. E. Denton, "The scaling of collisionless, magnetic reconnection for large systems," Geophys. Res. Lett. **26**, 2163–2166 (1999).

[19]M. M. Kuznetsova, M. Hesse, and D. Winske, "Toward a transport model of collisionless magnetic reconnection," J. Geophys. Res. **105**, 7601 (2000).

[20]M. M. Kuznetsova, M. Hesse, and D. Winske, "Collisionless reconnection supported by nongyrotropic pressure effects in hybrid and particle simulations," J. Geophys. Res. **106**, 3799–3810 (2001).

[21]F. Valentini, P. Trávníček, F. Califano, P. Hellinger, and A. Mangeney, "A hybrid-Vlasov model based on the current advance method for the simulation of collisionless magnetized plasma," J. Comput. Phys. **225**, 753–770 (2007).

[22]A. P. Matthews, "Current Advance Method and Cyclic Leapfrog for 2D Multispecies Hybrid Plasma Simulations," J. Comput. Phys. **112**, 102–116 (1994).

[23]F. Valentini, P. Veltri, F. Califano, and A. Mangeney, "Cross-Scale Effects in Solar-Wind Turbulence," Phys. Rev. Lett. **101**, 025006 (2008).

[24]F. Valentini, F. Califano, and P. Veltri, "Two-Dimensional Kinetic Turbulence in the Solar Wind," Phys. Rev. Lett. **104**, 205002 (2010).

[25]F. Valentini, D. Perrone, and P. Veltri, "Short-Wavelength Electrostatic Fluctuations In The Solar Wind," Astrophys. J. **739**, 54 (2011).

[26]J. Cheng, S. E. Parker, Y. Chen, and D. A. Uzdensky, "A second-order semi-implicit df method for hybrid simulation," J. Comput. Phys. **245**, 364–375 (2013).

[27]S. T. Jones and S. E. Parker, "Including electron inertia without advancing electron flow," J. Comput. Phys. **191**, 322–327 (2003).

[28]Y.-J. Su, S. T. Jones, R. E. Ergun, and S. E. Parker, "Modeling of field-aligned electron bursts by dispersive Alfvén waves in the dayside auroral region," J. Geophys. Res. **109**, A11201 (2004).

[29]Y.-J. Su, R. E. Ergun, S. T. Jones, R. J. Strangeway, C. C. Chaston, S. E. Parker, and J. L. Horwitz, "Generation of short-burst radiation through Alfvénic acceleration of auroral electrons," J. Geophys. Res. Space Phys. **112**, A06209 (2007).

[30]Y.-J. Su, S. T. Jones, R. E. Ergun, F. Bagenal, S. E. Parker, P. A. Delamere, and R. L. Lysak, "Io-Jupiter interaction: Alfvén wave propagation and ionospheric Alfvén resonator," J. Geophys. Res. **111**, A06211 (2006).

[31]T. Amano, K. Higashimori, and K. Shirakawa, "A robust method for handling low density regions in hybrid simulations for collisionless plasmas," J. Comput. Phys. **275**, 197–212 (2014), arXiv:1406.6613v1.

[32]D. S. Harned, "Quasineutral hybrid simulation of macroscopic plasma phenomena," J. Comput. Phys. **47**, 452–462 (1982).

[33]G. Lapenta, "Particle simulations of space weather," J. Comput. Phys. **231**, 795–821 (2012).

[34]P. Kilian, T. Burkart, and F. Spanier, "The Influence of the Mass Ratio on Particle Acceleration by the Filamentation Instability," in *High Performance Computing in Science and Engineering '11*, edited by W. E. Nagel, D. B. Kröner, and M. M. Resch (Springer Berlin Heidelberg, Berlin, Heidelberg, 2012) pp. 5–13.

[35]N. Jain, *Study of Electron-magnetohydrodynamic (EMHD) Phenomena in Plasmas*, Ph.d. thesis, Gujarat University (2006).

[36]N. Jain and J. Büchner, "Three dimensional instabilities of an electron scale current sheet in collisionless magnetic reconnection," Phys. Plasmas **21**, 062116 (2014).

[37]P. A. Muñoz and J. Büchner, "Non-Maxwellian electron distribution functions due to self-generated turbulence in collisionless guide-field reconnection," Phys. Plasmas **23**, 102103 (2016), arXiv:1608.03110.

[38]N. Jain and J. Büchner, "Effect of guide field on three-dimensional electron shear flow instabilities in electron current sheets," J. Plasma Phys. **81**, 905810606 (2015), arXiv:1411.3213v1.

[39]P. A. Muñoz, P. Kilian, and J. Büchner, "Instabilities of collisionless current sheets revisited: the role of anisotropic heating," Phys. Plasmas **21**, 112106 (2014), arXiv:1501.06022v1.

[40]T. Burkart, O. Elbracht, U. Ganse, and F. Spanier, "The influence of the mass-ratio on the acceleration of particles by filamentation instabilities," Astrophys. J. **720**, 1318–1324 (2010), arXiv:1007.1876.

[41]P. Kilian, *Teilchenbeschleunigung an kollisionsfreien Schockfronten*, Ph.d thesis (in german), University of Würzburg (2015).

[42]U. Ganse, P. Kilian, F. Spanier, and R. Vainio, "Fundamental and harmonic plasma emission in different plasma environments," Astron. Astrophys. **564**, 15 (2014), arXiv:1403.2240.

[43]C. Schreiner and F. Spanier, "Wave-particle-interaction in kinetic plasmas," Comput. Phys. Commun. **185**, 1981–1986 (2014), arXiv:arXiv:1404.0499v1.

[44]K. S. Yee, "Numerical solution of initial boundary value problems involving Maxwell's equations in isotropic media," IEEE Trans. Antennas Propag. **14**, 302–307 (1966).

[45]J. P. Boris, "Relativistic Plasma Simulation - Optimization of a Hybrid Code," in *Proceedings of the Fourth Conference on the Numerical Simulation of Plasmas, Washington DC*, edited by J. Boris (Naval Research Laboratory, 1970) pp. 3–67.

[46]J.-L. Vay, C. G. R. Geddes, E. Cormier-Michel, and D. Grote, "Numerical methods for instability mitigation in the modeling of laser wakefield accelerators in a Lorentz-boosted frame," J. Comput. Phys. **230**, 5908–5929 (2011).

[47]T. Esirkepov, "Exact charge conservation scheme for Particle-in-Cell simulation with an arbitrary form-factor," Comput. Phys. Commun. **135**, 144–153 (2001).

[48]Other hybrid codes have used this method due to other reasons. For example, the hybrid code by Ref. 16 implemented a charge preserving scheme[76] because it was computationally convenient for his curvilinear coordinate system.

[49]E. Cormier-Michel, B. Shadwick, C. G. R. Geddes, E. Esarey, C. B. Schroeder, and W. Leemans, "Unphysical kinetic effects in particle-in-cell modeling of laser wakefield accelerators," Phys. Rev. E **78**, 016404 (2008).

[50]J. Boris, A. Landsberg, E. Oran, and J. Gardner, "LCPFCT - A Flux-Corrected Transport Algorithm for Solving Generalized Continuity Equations," Tech. Rep. (NRL Memorandum Report 93-7192, 1993).

[51]`http://www.nrl.navy.mil/lcp/LCPFCT`.

[52]`https://www2.cisl.ucar.edu/resources/legacy/mudpack`.

[53]J. C. Adams, "mudpack: Multigrid portable fortran software for the efficient solution of linear elliptic partial differential equations," Appl. Math. Comput. **34**, 113–146 (1989).

[54]J. C. Adams, "Recent enhancements in MUDPACK, a multigrid software package for elliptic partial differential equations," Appl. Math. Comput. **43**, 79–93 (1991).

[55]T. Boyd and J. Sanderson, *The Physics of Plasmas* (Cambridge University Press, 2003).

[56]W. Baumjohann and R. A. Treumann, *Basic Space Plasma Physics* (Imperial College Press

; Distributed by World Scientific Pub., 1997).

[57]T. Terasawa, M. Hoshino, J.-I. Sakai, and T. Hada, "Decay instability of finite-amplitude circularly polarized Alfven waves: A numerical simulation of stimulated Brillouin scattering," J. Geophys. Res. **91**, 4171 (1986).

[58]A. Langdon, "Effects of the spatial grid in simulation plasmas," J. Comput. Phys. **6**, 247–267 (1970).

[59]M. Melzani, C. Winisdoerffer, R. Walder, D. Folini, J. M. Favre, S. Krastanov, and P. Messmer, "Apar-T: code, validation, and physical interpretation of particle-in-cell results," Astron. Astrophys. **558**, A133 (2013).

[60]J. A. Araneda, H. Astudillo, and E. Marsch, "Interactions of Alfvén-Cyclotron Waves with Ions in the Solar Wind," Space Sci. Rev. **172**, 361–372 (2012).

[61]S. P. Gary, *Theory of space plasma microinstabilities* (Cambridge University Press, 1993).

[62]I. Bernstein, "Waves in a Plasma in a Magnetic Field," Phys. Rev. **109**, 10–21 (1958).

[63]J. J. Rasmussen, "Electrostatic Waves and Instabilities in Homogeneous, Magnetized Plasmas," in *Waves and Instabilities in Plasmas*, edited by F. Cap (Springer Vienna, 1994) Chap. 4, pp. 117–170.

[64]D. Winske and M. M. Leroy, "Diffuse ions produced by electromagnetic ion beam instabilities," J. Geophys. Res. **89**, 2673 (1984).

[65]H. Matsumoto and Y. Omura, *Computer Space Plasma Physics : Simulation Techniques and Software* (Terra Scientific Publishing Company, 1993).

[66]L. D. Landau, "On the vibrations of the electronic plasma," J. Phys. USSR **10**, 25 (1946).

[67]M. W. Kunz, J. M. Stone, and X.-N. Bai, "Pegasus: A new hybrid-kinetic particle-in-cell code for astrophysical plasma dynamics," J. Comput. Phys. **259**, 154–174 (2014), arXiv:1311.4865v1.

[68]B. D. Fried and S. D. Conte, *The Plasma Dispersion Function: the Hilbert transform of the Gaussian* (Academic Press, 1961).

[69]G. Manfredi, "Long-Time Behavior of Nonlinear Landau Damping," Phys. Rev. Lett. **79**, 2815–2818 (1997).

[70]P. Rambo, "Finite-Grid Instability in Quasineutral Hybrid Simulations," J. Comput. Phys. **118**, 152–158 (1995).

[71]P. Rambo, "Numerical Heating in Hybrid Plasma Simulations," J. Comput. Phys. **133**, 173–180 (1997).

[72]R. A. Treumann and W. Baumjohann, *Advanced Space Plasma Physics* (Published by Imperial College Press and distributed by World Scientific Publishing Co., 2001).

[73]P. H. Yoon, C. S. Wu, and A. S. de Assis, "Effect of finite ion gyroradius on the fire-hose instability in a high beta plasma," Phys. Fluids B Plasma Phys. **5**, 1971 (1993).

[74]P. Hellinger and H. Matsumoto, "Nonlinear competition between the whistler and Alfvén fire hoses," J. Geophys. Res. Space Phys. **106**, 13215–13218 (2001).

[75]P. Hellinger and H. Matsumoto, "New kinetic instability: Oblique Alfvén fire hose," J. Geophys. Res. Space Phys. **105**, 10519–10526 (2000).

[76]J. Villasenor and O. Buneman, "Rigorous charge conservation for local electromagnetic field solvers," Comput. Phys. Commun. **69**, 306–316 (1992).